

---

## 6. Aerodynamics of 3D Lifting Surfaces through Vortex Lattice Methods

### 6.1 An Introduction

There is a method that is similar to panel methods but very easy to use and capable of providing remarkable insight into wing aerodynamics and component interaction. It is the vortex lattice method (**vlm**), and was among the earliest methods utilizing computers to actually assist aerodynamicists in estimating aircraft aerodynamics. Vortex lattice methods are based on solutions to Laplace's Equation, and are subject to the same basic theoretical restrictions that apply to panel methods.

As a comparison, vortex lattice methods are:

*Similar to Panel methods:*

- singularities are placed on a surface
- the non-penetration condition is satisfied at a number of control points
- a system of linear algebraic equations is solved to determine singularity strengths

*Different from Panel methods:*

- Oriented toward lifting effects, and classical formulations ignore thickness
- Boundary conditions (BCs) are applied on a mean surface, not the actual surface (not an exact solution of Laplace's equation over a body, but embodies some additional approximations, *i.e.*, together with the first item, we find  $C_p$ , not  $C_{pupper}$  and  $C_{plower}$ )
- Singularities are not distributed over the entire surface
- Oriented toward combinations of thin lifting surfaces (recall Panel methods had no limitations on thickness).

Vortex lattice methods were first formulated in the late '30s, and the method was first called "Vortex Lattice" in 1943 by Faulkner. The concept is extremely simple, but because of its purely numerical approach (*i.e.*, no answers are available at all without finding the numerical solution of a matrix too large for routine hand calculation) practical applications awaited sufficient development of computers—the early '60s saw widespread adoption of the method. A workshop was devoted to these methods at NASA in the mid '70s.<sup>1</sup> A nearly universal standard for vortex lattice predictions was established by a code developed at NASA Langley (the various versions were available prior to the report dates):

|                                |                    |                |      |
|--------------------------------|--------------------|----------------|------|
| Margason & Lamar <sup>2</sup>  | 1st Langley report | NASA TN D-6142 | 1971 |
| Lamar & Gloss <sup>3</sup>     | 2nd " "            | NASA TN D-7921 | 1975 |
| Lamar & Herbert <sup>4,5</sup> | 3rd " "            | NASA TM 83303  | 1982 |

Each new version had considerably more capability than the previous version. The “final” development in this series is designated VLM4.997. The original codes could handle two lifting surfaces, while VLM4.997 could handle four. Many, many other people have written vortex lattice method codes, some possibly even better than the code described in the NASA reports. But the NASA code’s general availability, versatility, and reliability resulted in its becoming a de-facto standard.

Some of the most noteworthy variations on the basic method have been developed by Lan<sup>6</sup> (Quasi-Vortex Lattice Method), Hough<sup>7</sup>, DeJarnette<sup>8</sup> and Frink<sup>9</sup>. Mook<sup>10</sup> and co-workers at Virginia Tech have developed vortex lattice class methods that treat flowfields that contain leading edge vortex type separation (see Section 6.12) and also handle general unsteady motions. The recent book by Katz and Plotkin<sup>11</sup> contains another variation. At Virginia Tech, Jacob Kay wrote a code using the method of Katz and Plotkin to estimate stability derivatives, which is available from the department web page.<sup>12</sup>

To understand the method, a number of basic concepts must be reviewed. Then we describe one implementation of the **vlm** method, and use it to obtain insights into wing and wing-canard aerodynamics. Naturally, the method is based on the idea of a vortex singularity as the solution of Laplace’s equation. A good description of the basic theory for vortices in inviscid flow and thin wing analysis is contained in Karamcheti,<sup>13</sup> pp. 494-496, 499-500, and 518-534. A good description of the vortex lattice method is given by Bertin and Smith.<sup>14</sup> After the discussion of wing and wing-canard aerodynamics, an example of a vortex lattice method used in a design mode is presented, where the camber line required to produce a specified loading is found. The chapter concludes with a few examples of the extension of vortex lattice methods to treat situations with more complicated flowfields than the method was originally intended to treat.

### **6.2 Boundary conditions on the mean surface and the pressure relation**

An important difference between vortex lattice methods and panel methods is the method in which the boundary conditions are handled. Typically, the vortex lattice method uses an approximate boundary condition treatment. This boundary condition can also be used in other circumstances to good advantage. This is a good “trick” applied aerodynamicists should know and understand. In general, this approach results in the so-called “thin airfoil boundary condition,” and arises by linearizing and transferring the boundary condition from the actual surface to a flat mean “reference” surface, which is typically a constant coordinate surface. Consistent with the boundary condition simplification, a simplified relation between the pressure and velocity is also possible. The simplification in the boundary condition and pressure-velocity relation provides a basis for treating the problem as a superposition of the lift and thickness contributions to the aerodynamic results. Karamcheti<sup>13</sup> provides an excellent discussion of this approach.

To understand the thin airfoil theory boundary condition treatment, we provide an example in two dimensions. Recall (from Eqn. 2-54) that the exact surface boundary condition for steady inviscid flow is:

$$\mathbf{V} \cdot \mathbf{n} = 0 \tag{6-1}$$

on  $F(x, y) = 0 = y - f(x)$ . The unit normal vector is  $\mathbf{n} = \nabla F(x, y) / |\nabla F(x, y)|$  and the velocity field is defined using the notation defined in Fig. 6-1.

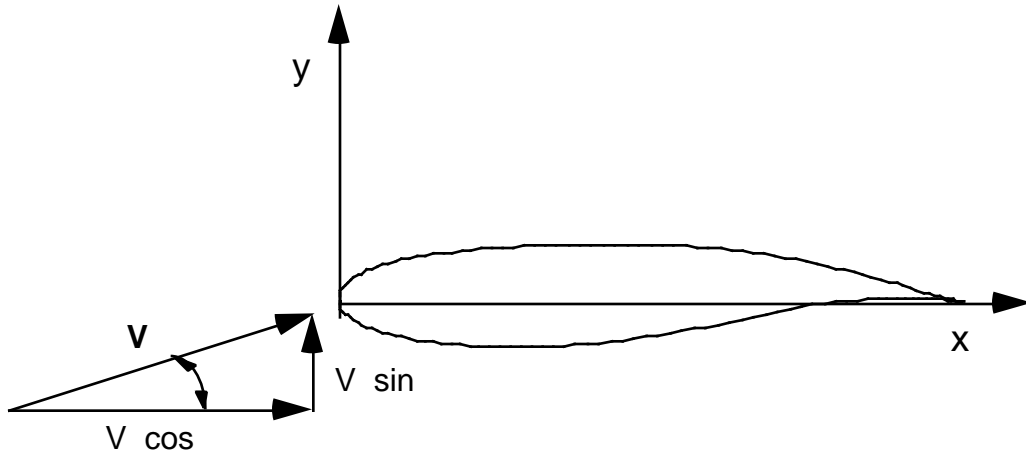


Figure 6-1. Basic coordinate system for boundary condition analysis.

Define the velocity components of  $\mathbf{V}$  as:

$$\mathbf{V} = \mathbf{V} + \underbrace{\mathbf{q}(x, y)}_{\text{a disturbance velocity}} \tag{6-2}$$

where  $\mathbf{q}$  is a disturbance velocity with components  $u$  and  $v$ . If we assume irrotational flow, then these components are described in terms of a scalar potential function,  $u = \frac{\partial \phi}{\partial x}$  and  $v = \frac{\partial \phi}{\partial y}$ . The total velocity  $\mathbf{V}$  then becomes in terms of velocity components:

$$\begin{aligned} u_{\text{TOT}} &= V \cos \alpha + u(x, y) \\ v_{\text{TOT}} &= V \sin \alpha + v(x, y) \end{aligned} \tag{6-3}$$

and we can write out the boundary condition as:

$$\mathbf{V} \cdot \mathbf{n} = (u_{\text{TOT}} \mathbf{i} + v_{\text{TOT}} \mathbf{j}) \cdot \left( \frac{\partial F}{\partial x} \mathbf{i} + \frac{\partial F}{\partial y} \mathbf{j} \right) = 0 \tag{6-4}$$

or

$$\left[ V \cos \alpha + u(x, y) \right] \frac{\partial F}{\partial x} + \left[ V \sin \alpha + v(x, y) \right] \frac{\partial F}{\partial y} = 0 \tag{6-5}$$

on  $F(x, y) = 0$ , and recalling the relationship between  $F$  and  $f$  given below Eqn. (6-1):

$$\frac{F}{x} = -\frac{1}{x}\{y - f(x)\} = -\frac{df(x)}{dx}$$

$$\frac{F}{y} = -\frac{1}{y}\{y - f(x)\} = 1$$
(6-7)

Substituting for  $F$  in Eq.(6-5) we have:

$$(V \cos \alpha + u) - \frac{df}{dx} + (V \sin \alpha + v) = 0$$
(6-8)

which, solving for  $v$ , is:

$$v = (V \cos \alpha + u) \frac{df}{dx} - V \sin \alpha$$
(6-9)

on  $y = f(x)$ . Note that  $v$  is defined in terms of the unknown  $u$ . Thus Eq. (6-9) is a nonlinear boundary condition and further analysis is needed to obtain a useful relation.\*

### 6.2.1 Linearized form of the boundary condition

The relation given above by Eq.(6-9) is exact. It has been derived as the starting point for the derivation of useful relations when the body (which is assumed to be a thin surface at a small angle of attack) induces disturbances to the freestream velocity that are small in comparison to the freestream velocity. Thus we assume:  $u \ll V$ ,  $v \ll V$ , and  $F/x \ll F/y$ . Note that this introduces a bias in the coordinate system to simplify the analysis, a typical consequence of introducing simplifying assumptions. Consistent with this assumption, the components of the freestream velocity are:

$$\begin{aligned} V \cos \alpha & \approx V \\ V \sin \alpha & \approx V \alpha \end{aligned}$$
(6-10)

and the expression for  $v$  in Eq.(6-9) becomes:

$$v = (V + u) \frac{df}{dx} - V \alpha$$
(6-11)

Dividing by  $V$ ,

$$\frac{v}{V} = 1 + \frac{u}{V} \frac{df}{dx} - \alpha$$
(6-12)

the linearized boundary condition is obtained by neglecting  $u/V$  compared with unity (consistent with the previous approximations). With this assumption, the linearized boundary condition becomes:

$$\frac{v}{V} = \frac{df}{dx} - \alpha \quad \text{on } y = f(x)$$
(6-13)

---

\* Observe that even when the flowfield model is defined by a linear partial differential equation, an assumption which we have not yet made, the boundary condition can make the problem nonlinear.

This form of the boundary condition is not valid if the flow disturbance is large compared to the freestream velocity {for aerodynamically streamlined shapes this is usually valid everywhere except at the leading edge of the airfoil, where a stagnation point exists ( $u = -V$ ) and the slope is infinite ( $df/dx = \infty$ )}. In practice, a local violation of this assumption leads to a local error. Thus, if the details of the flow at the leading edge are not important to the analysis, which surprisingly is often the case, the linearized boundary condition can be used.

### 6.2.2 Transfer of the boundary condition

Although Eqn. (6-13) is linear, it's hard to apply because it is not applied on a coordinate line.\* We now use a further approximation of this relation to get the useful form of the linearized boundary condition. Using a Taylor series expansion of the  $v$  component of velocity about the coordinate axis we obtain the  $v$  velocity on the surface:

$$v\{x, y = f(x)\} = v(x, 0) + f(x) \left. \frac{dv}{dy} \right|_{y=0} + \dots \quad (6-14)$$

For the thin surfaces under consideration,  $f(x)$  is small, and because the disturbances are assumed small,  $v/y$  is also small. For example, assume that  $v$  and  $v/y$  are the same size, equal to 0.1, and  $df/dy$  is also about 0.1. The relation between  $v$  on the airfoil surface and the axis is:

$$v\{x, y = f(x)\} = (.1) + (.1)(.1) = .1 + \underbrace{.01}_{\text{neglect}} \quad (6-15)$$

Neglecting the second term, we assume:

$$v\{x, f(x)\} = v(x, 0). \quad (6-16)$$

We now apply both the upper and lower surface boundary conditions on the axis  $y = 0$ , and distinguish between the upper and lower surface shapes by using:

$$\begin{aligned} f &= f_u && \text{on the upper surface} \\ f &= f_l && \text{on the lower surface} \end{aligned} \quad (6-17)$$

Using Eq. (6-17), we write the upper and lower surface boundary conditions as:

$$\left. \frac{v(x, 0^+)}{V} \right|_{up} = \frac{df_u}{dx} \quad , \quad \left. \frac{v(x, 0^-)}{V} \right|_{low} = \frac{df_l}{dx} \quad (6-18)$$

---

\* The simplification introduced by applying boundary conditions on constant coordinate surfaces justifies the use of rather elaborate transformations, which will be discussed in more detail in Chap. 9, Geometry and Aerodynamics.

These are the linearized and transferred boundary conditions. Frequently, these boundary conditions result in a surprisingly good approximation to the flowfield, even in transonic and supersonic flow.

### 6.2.3 Decomposition of boundary conditions to camber/thickness/alpha

Further simplification and insight can be gained by considering the airfoils in terms of the combination of thickness and camber, a natural point of view. We thus write the upper and lower surface shapes in terms of camber,  $f_c$ , and thickness,  $f_t$ , as:

$$\begin{aligned} f_u &= f_c + f_t \\ f_l &= f_c - f_t \end{aligned} \quad (6-19)$$

and the general problem is then divided into the sum of three parts as shown in Fig. 6-2.

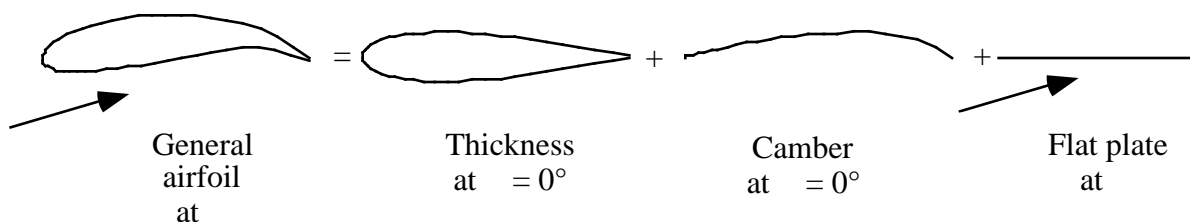


Figure 6-2. Decomposition of a general shape at incidence.

The decomposition of the problem is somewhat arbitrary. Camber could also be considered to include angle of attack effects using the boundary condition relations given above, the sign is the same for both the upper and lower surface. The aerodynamicist must keep track of details for a particular problem. *To proceed further, we make use of the basic vortex lattice method assumption: the flowfield is governed by a linear partial differential equation (Laplace's equation).* Superposition allows us to solve the problem in pieces and add up the contributions from the various parts of the problem. This results in the final form of the thin airfoil theory boundary conditions:

$$\begin{aligned} \left. \frac{v(x, 0^+)}{V} \right|_{up} &= \frac{df_c}{dx} + \frac{df_t}{dx} - \\ \left. \frac{v(x, 0^-)}{V} \right|_{low} &= \frac{df_c}{dx} - \frac{df_t}{dx} - \end{aligned} \quad (6-20)$$

The problem can be solved for the various contributions and the contributions are added together to obtain the complete solution. If thickness is neglected the boundary conditions are the same for the upper and lower surface.

6.2.4 Thin airfoil theory pressure relation

Consistent with the linearization of the boundary conditions, a useful relation between the pressure and velocity can also be obtained. For incompressible flows, the exact relation between pressure and velocity is:

$$C_p = 1 - \frac{V^2}{V_\infty^2} \tag{6-21}$$

and we expand the velocity considering disturbances to the freestream velocity using the approximations discussed above:

$$V^2 = (V \cos \alpha + u)^2 + (V \sin \alpha + v)^2$$

Expanding:

$$V^2 = V^2 + 2V u + u^2 + (V \sin \alpha)^2 + 2V v + v^2 \tag{6-22}$$

and dividing by  $V_\infty^2$  we get:

$$\frac{V^2}{V_\infty^2} = 1 + 2\frac{u}{V_\infty} + \frac{u^2}{V_\infty^2} + \sin^2 \alpha + 2\frac{v}{V_\infty} + \frac{v^2}{V_\infty^2} \tag{6-23}$$

Substituting into the  $C_p$  relation, Eqn. (6-21), we get:

$$\begin{aligned} C_p &= 1 - \left[ 1 + 2\frac{u}{V_\infty} + \frac{u^2}{V_\infty^2} + \sin^2 \alpha + 2\frac{v}{V_\infty} + \frac{v^2}{V_\infty^2} \right] \\ &= 1 - 1 - 2\frac{u}{V_\infty} - \frac{u^2}{V_\infty^2} - \sin^2 \alpha - 2\frac{v}{V_\infty} - \frac{v^2}{V_\infty^2} \end{aligned} \tag{6-24}$$

and if  $\alpha$ ,  $u/V_\infty$  and  $v/V_\infty$  are  $\ll 1$ , then the last four terms can be neglected in comparison with the third term. The final result is:

$$C_p = -2\frac{u}{V_\infty} \tag{6-25}$$

This is the linearized or “thin airfoil theory pressure formula”. From experience gained comparing various computational results, I’ve found that this formula is a slightly more severe restriction on the accuracy of the solution than the linearized boundary condition. Equation (6-25) shows that under the small disturbance approximation, the pressure is a linear function of  $u$ , and we can add the  $C_p$  contribution from thickness, camber, and angle of attack by superposition. A similar derivation can be used to show that Eq. (6-25) is also valid for compressible flow up to moderate supersonic speeds.

## 6.2.5 Delta Cp due to camber/alpha (thickness cancels)

Next, we make use of the result in Eq. (6-25) to obtain a formula for the load distribution on the wing:

$$C_p = C_{p_{\text{LOWER}}} - C_{p_{\text{UPPER}}} \quad (6-26)$$

Using superposition, the pressures can be obtained as the contributions from wing thickness, camber, and angle of attack effects:

$$\begin{aligned} C_{p_{\text{LOWER}}} &= C_{p_{\text{THICKNESS}}} + C_{p_{\text{CAMBER}}} + C_{p_{\text{ANGLE OF ATTACK}}} \\ C_{p_{\text{UPPER}}} &= C_{p_{\text{THICKNESS}}} - C_{p_{\text{CAMBER}}} - C_{p_{\text{ANGLE OF ATTACK}}} \end{aligned} \quad (6-27)$$

so that:

$$\begin{aligned} C_p &= \left( C_{p_{\text{THICKNESS}}} + C_{p_{\text{CAMBER}}} + C_{p_{\text{ANGLE OF ATTACK}}} \right) \\ &\quad - \left( C_{p_{\text{THICKNESS}}} - C_{p_{\text{CAMBER}}} - C_{p_{\text{ANGLE OF ATTACK}}} \right) \\ &= 2 \left( C_{p_{\text{CAMBER}}} + C_{p_{\text{ANGLE OF ATTACK}}} \right) \end{aligned} \quad (6-28)$$

Equation (6-28) demonstrates that for cases where the linearized pressure coefficient relation is valid, *thickness does not contribute to lift to 1<sup>st</sup> order in the velocity disturbance!*

The importance of this analysis is that we have shown:

1. how the lifting effects can be obtained without considering thickness, and
2. that the cambered surface boundary conditions can be applied on a flat coordinate surface, resulting in an easy to apply boundary condition.

The principles demonstrated here for transfer and linearization of boundary conditions can be applied in a variety of situations other than the application in vortex lattice methods. Often this idea can be used to handle complicated geometries that can't easily be treated exactly.

The analysis here produced an entirely consistent problem formulation. This includes the linearization of the boundary condition, the transfer of the boundary condition, and the approximation between velocity and pressure. All approximations are consistent with each other. Improving one of these approximations without improving them all in a consistent manner may actually lead to worse results. Sometimes you can make agreement with data better, sometimes it may get worse. You have to be careful when trying to improve theory on an *ad hoc* basis.

### 6.3 Vortex Theorems

In using vortex singularities to model lifting surfaces, we need to review some properties of vortices. The key properties are defined by the so-called vortex theorems. These theorems are associated with the names of Kelvin and Helmholtz, and are proven in Karamcheti.<sup>13</sup> Three important results are:

1. Along a vortex line (tube) the circulation,  $\Gamma$ , is constant.
2. A vortex filament (or line) cannot begin or end abruptly in a fluid. The vortex line must i) be closed, ii) extend to infinity, or iii) end at a solid boundary. Furthermore, the circulation,  $\Gamma$ , about any section is the vortex strength.
3. An initially irrotational, inviscid flow will remain irrotational.

Related to these theorems we state an important result:

- A sheet of vortices can support a jump in tangential velocity [i.e. a force], while the normal velocity is continuous. This means you can use a vortex sheet to represent a lifting surface.

### 6.4 Biot-Savart Law

We know that a two-dimensional vortex singularity satisfies Laplace's equation (i.e. a point vortex):

$$\mathbf{V} = \frac{\Gamma}{2\pi r} \mathbf{e}_\theta \quad (6-29)$$

where  $V$  is the irrotational vortex flow illustrated in Fig. 6-3.

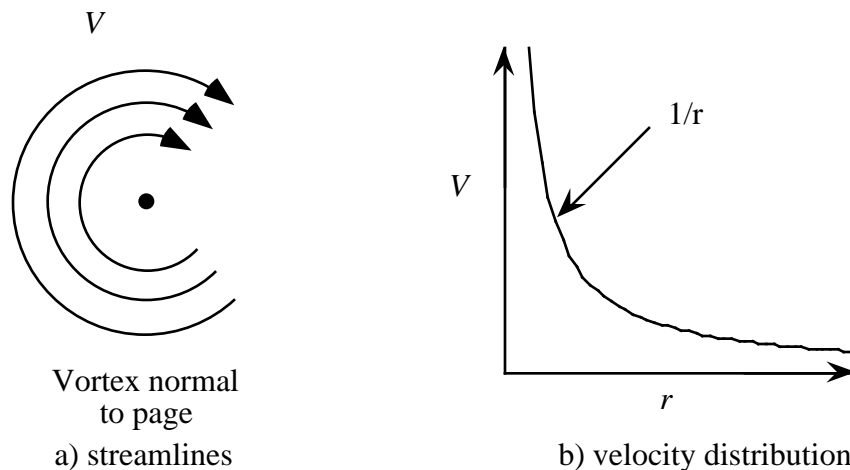


Figure 6-3. The point vortex.

What is the extension of the point vortex idea to the case of a general three-dimensional vortex filament? Consider the flowfield induced by the vortex filament shown in Fig. 6-4, which defines the nomenclature.

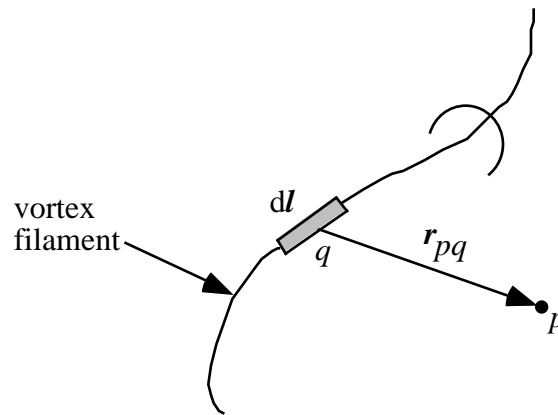


Figure 6-4. General three-dimensional vortex filament.

The mathematical description of the flow induced by this filament is given by the Biot-Savart law (see Karamcheti,<sup>13</sup> pages 518-534). It states that the increment in velocity  $d\mathbf{V}$  at a point  $p$  due to a segment of a vortex filament  $d\mathbf{l}$  at  $q$  is:

$$d\mathbf{V}_p = \frac{d\mathbf{l} \times \mathbf{r}_{pq}}{4 |\mathbf{r}_{pq}|^3}. \quad (6-30)$$

To obtain the velocity induced by the entire length of the filament, integrate over the length of the vortex filament (or line) recalling that  $\Gamma$  is constant. We obtain:

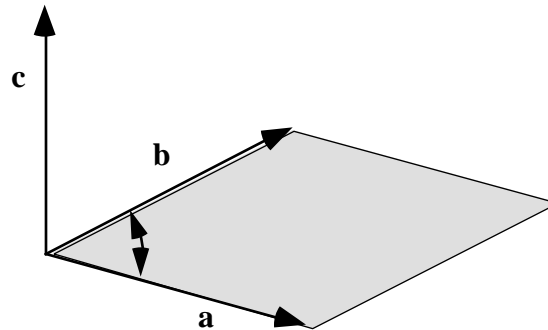
$$\vec{V}_p = \frac{\Gamma}{4} \frac{d\vec{l} \times \vec{r}_{pq}}{|\vec{r}_{pq}|^3}. \quad (6-31)$$

To illustrate the evaluation of this integral we give the details for several important examples. The vector cross product definition is reviewed in the sidebar below. Reviewing the cross product properties we see that the velocity direction  $d\mathbf{V}_p$  induced by the segment of the vortex filament  $d\mathbf{l}$  is perpendicular to the plane defined by  $d\mathbf{l}$  and  $\mathbf{r}_{pq}$ , and its magnitude is computed from Eq. (6-31).

*Case #1: the infinitely long straight vortex.*

In the first illustration of the computation of the induced velocity using the Biot-Savart Law, we consider the case of an infinitely long straight vortex filament. The notation is given in Fig. 6-5.

A review: the meaning of the cross product. What does  $\mathbf{a} \times \mathbf{b}$  mean? Consider the following sketch:



Here, the vectors  $\mathbf{a}$  and  $\mathbf{b}$  form a plane, and the result of the cross product operation is a vector  $\mathbf{c}$ , where  $\mathbf{c}$  is perpendicular to the plane defined by  $\mathbf{a}$  and  $\mathbf{b}$ . The value is given by:

$$\mathbf{c} = \mathbf{a} \times \mathbf{b} = |\mathbf{a}||\mathbf{b}|\sin \theta$$

and  $\theta$  is perpendicular to the plane of  $\mathbf{a}$  and  $\mathbf{b}$ . One consequence of this is that if  $\mathbf{a}$  and  $\mathbf{b}$  are parallel, then  $\mathbf{a} \times \mathbf{b} = 0$ .

Also:  $|\mathbf{a} \times \mathbf{b}| = \text{area of the parallelogram}$

and

$$\mathbf{a} \times \mathbf{b} = \begin{vmatrix} \mathbf{i} & \mathbf{j} & \mathbf{k} \\ A_x & A_y & A_z \\ B_x & B_y & B_z \end{vmatrix} = (A_y B_z - A_z B_y)\mathbf{i} - (A_x B_z - A_z B_x)\mathbf{j} + (A_x B_y - A_y B_x)\mathbf{k}$$

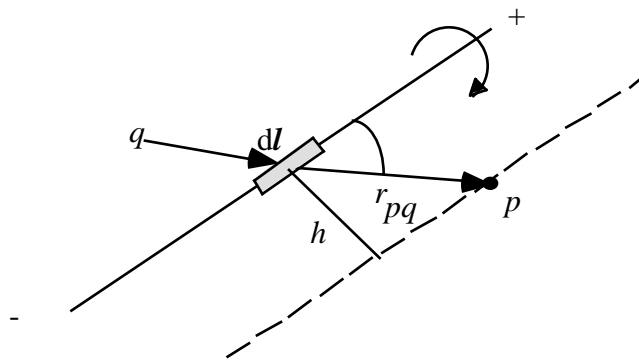


Figure 6-5. The infinitely long straight vortex.

## 6 - 12 Applied Computational Aerodynamics

Now consider the numerator in Eq. (6-30) given above using the definition of the cross product:

$$d\mathbf{l} \times \mathbf{r}_{pq} = |d\mathbf{l}| |\mathbf{r}_{pq}| \sin \theta \frac{\mathbf{V}}{|\mathbf{V}|} \quad (6-32)$$

so that the entire expression becomes

$$\begin{aligned} d\mathbf{V}_p &= \frac{1}{4} \frac{|d\mathbf{l}| |\mathbf{r}_{pq}| \sin \theta}{|\mathbf{r}_{pq}|^3} \frac{\mathbf{V}}{|\mathbf{V}|} \\ &= \frac{1}{4} \frac{\mathbf{V} \sin \theta}{|\mathbf{V}|} \frac{dl}{r_{pq}^2} \end{aligned} \quad (6-33)$$

Next, simplify the above expressions so they can be readily evaluated. Use the nomenclature shown in Fig. 6-6.

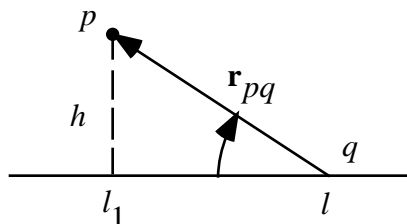


Figure 6-6. Relations for the solution of the Biot-Savart Law.

Using the notation in Fig. 6-6 to find the relations for  $\mathbf{r}_{pq}$  and  $d\mathbf{l}$ . First we see that:

$$h = r_{pq} \sin \theta \quad (6-34)$$

or 
$$r_{pq} = \frac{h}{\sin \theta} \quad (6-35)$$

and 
$$l_1 - l = \frac{h}{\tan \theta} = h \cot \theta \quad (6-36)$$

Next look at changes with  $\theta$ . Start by taking the differential of Eq. (6-36):

$$d(l_1 - l) = d \left( \frac{h}{\tan \theta} \right) = d(h \cot \theta)$$

which is 
$$-dl = h d(\cot \theta) \quad (6-37)$$

$$-\frac{dl}{d\theta} = h \frac{d}{d\theta} (\cot \theta) = -h \operatorname{cosec}^2 \theta$$

and we can now write  $dl$  in terms of  $d\theta$ :

$$dl = h \operatorname{cosec}^2 \theta d\theta \quad (6-38)$$

so that the Biot-Savart Law gives:

$$\begin{aligned}
 d\mathbf{V}_p &= \frac{\mathbf{V}}{4} \frac{\sin dl}{|\mathbf{V}| r_{pq}^2} \\
 &= \frac{\mathbf{V}}{4} \frac{\sin h \operatorname{cosec}^2 d}{|\mathbf{V}| \frac{h}{\sin}^2} \quad (6-39) \\
 &= \frac{\sin}{4} \frac{d}{h} \quad (\text{direction understood})
 \end{aligned}$$

Thus we integrate:

$$\mathbf{V}_p = \frac{\sin}{4} \frac{d}{h} \Big|_{=0}^{\quad} = \frac{\sin}{4} \frac{d}{h} \quad (6-40)$$

where here the limits of integration would change if you were to consider a finite straight length.

Carrying out the integration:

$$\begin{aligned}
 \mathbf{V}_p &= \frac{1}{4} \frac{1}{h} [-\cos \theta]_{=0}^{\quad} \\
 &= \frac{1}{4} \frac{1}{h} [ -(-1) - (-1) ]
 \end{aligned}$$

and:

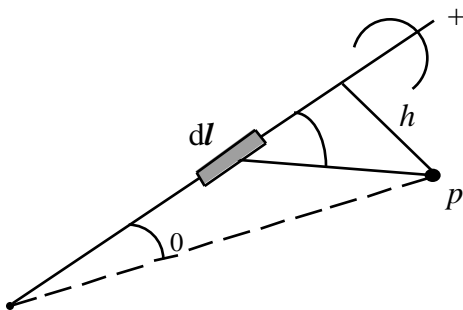
$$\mathbf{V}_p = \frac{1}{2} \frac{\mathbf{V}}{h} \quad (6-41)$$

which agrees with the two dimensional result.

Although a vortex cannot end in a fluid, we can construct expressions for infinitely long vortex lines made up of a series of connected straight line segments by combining expressions developed using the method illustrated here. To do this we simply change the limits of integration. Two cases are extremely useful for construction of vortex systems, and the formulas are given here without derivation.

*Case #2: the semi-infinite vortex.*

This expression is useful for modeling the vortex extending from the wing to downstream infinity.

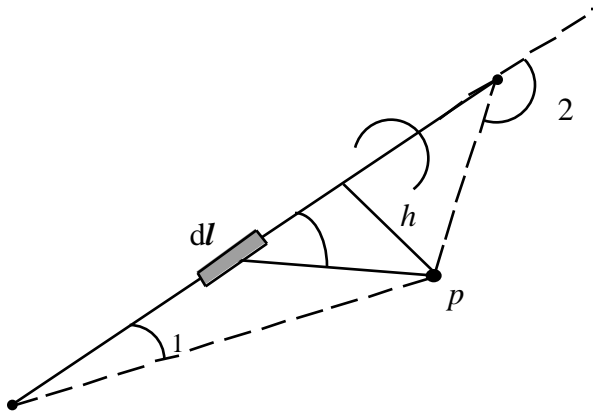


$$\mathbf{V}_p = \frac{\mathbf{V}}{4} \frac{1}{h} (1 + \cos \theta) \mathbf{e} \quad (6-42)$$

Figure 6-7. The semi-infinite vortex.

*Case #3: the finite vortex.*

This expression can be used to model the vortex on a wing, and can be joined with two semi-infinite vortices to form a vortex of infinite length, satisfying the vortex theorems.



$$\mathbf{V}_p = \frac{\Gamma}{4h} (\cos \alpha_1 - \cos \alpha_2) \mathbf{e} \quad (6-43)$$

Figure 6-8. The finite vortex.

Systems of vortices can be built up using Eqns. (6-42) and (6-43) and the vortex theorems. The algebra can become tedious, but there are no conceptual difficulties.

### 6.5 The Horseshoe Vortex

There is a specific form of vortex used in the traditional vortex lattice method. We now use the expressions developed from the Biot-Savart Law to create a “horseshoe vortex”, which extends from downstream infinity to a point in the field “A”, then from point “A” to point “B,” and another vortex from point “B” downstream to infinity. The velocity induced by this vortex is the sum of the three parts. The basic formulas were presented in the previous section. Here we extend the analysis of the previous section, following the derivation and notation of Bertin and Smith.<sup>14</sup> In particular, the directions of the induced flow are made more precise. Our goal is to obtain the expression for the velocity field at a general point in space  $(x,y,z)$  due to the specified horseshoe vortex.

To create a horseshoe vortex we will use three straight line vortices: one finite length vortex and two semi-infinite vortices. This is illustrated in Fig. 6-9. To start our analysis, we rewrite the Biot-Savart Law in the Bertin and Smith notation,<sup>14</sup> which is given in Fig. 6-10.

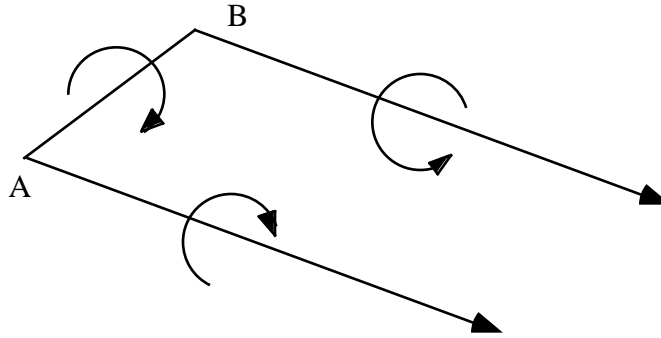


Figure 6-9. The horseshoe vortex.

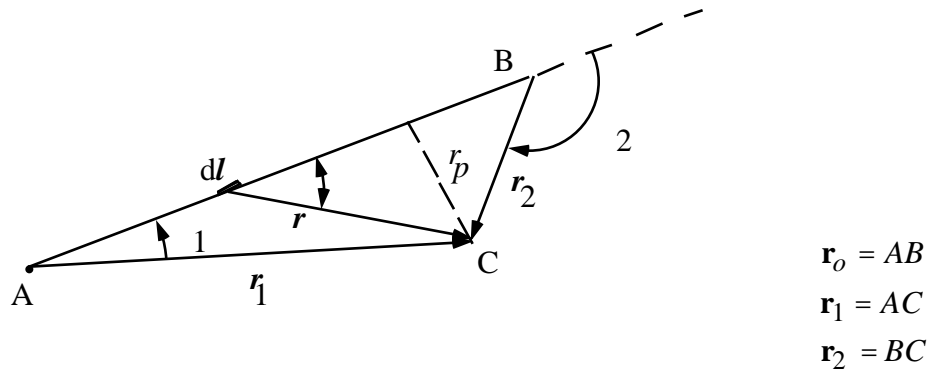


Figure 6-10. Nomenclature for induced velocity calculation.

The next step is to relate the angles to the vector definitions. The definition of the dot product is used:

$$\mathbf{A} \cdot \mathbf{B} = |\mathbf{A}||\mathbf{B}|\cos \theta \tag{6-44}$$

so that:

$$\cos \theta_1 = \frac{\mathbf{r}_0 \cdot \mathbf{r}_1}{|\mathbf{r}_0||\mathbf{r}_1|} \tag{6-45}$$

$$\cos \theta_2 = \frac{\mathbf{r}_0 \cdot \mathbf{r}_2}{|\mathbf{r}_0||\mathbf{r}_2|}$$

Next, we put these relations into the formula for the finite length vortex segment formula for the induced velocity field given above in Eq. (6-43).

$$\mathbf{V}_p = \frac{\Gamma}{4|\mathbf{r}_p|} (\cos \theta_1 - \cos \theta_2) \mathbf{e} \tag{6-46}$$

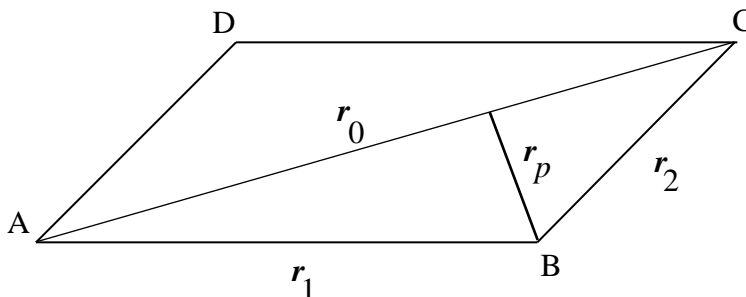
so that, substituting using the definition in Eq. (6-44), we get

$$\mathbf{V}_p = \frac{\Gamma}{4} \frac{|\mathbf{r}_0|}{|\mathbf{r}_1 \times \mathbf{r}_2|} \frac{\mathbf{r}_0 \cdot \mathbf{r}_1}{|\mathbf{r}_0||\mathbf{r}_1|} - \frac{\mathbf{r}_0 \cdot \mathbf{r}_2}{|\mathbf{r}_0||\mathbf{r}_2|} \frac{\mathbf{r}_1 \times \mathbf{r}_2}{|\mathbf{r}_1 \times \mathbf{r}_2|} \tag{6-47}$$

Bertin and Smith<sup>14</sup> use the relation:

$$|\mathbf{r}_p| = \frac{|\mathbf{r}_1 \times \mathbf{r}_2|}{|\mathbf{r}_0|} |\mathbf{r}_p| = \frac{|\mathbf{r}_1 \times \mathbf{r}_2|}{|\mathbf{r}_0|}$$

and we need to demonstrate that this is true. Consider the parallelogram ABCD shown in the sketch:



by definition:  $|\mathbf{r}_1 \times \mathbf{r}_2| = A_p$ , is the area of the parallelogram.

Similarly, the area of  $ABC$  is:

$$\begin{aligned} A_{ABC} &= \frac{1}{2} bh \\ &= \frac{1}{2} |\mathbf{r}_0| |\mathbf{r}_p| \end{aligned}$$

The total area of the parallelogram can be found from both formulas, and by equating these two areas we obtain the expression we are trying to get:

$$\begin{aligned} 2A_{ABC} &= A_p \\ |\mathbf{r}_0| |\mathbf{r}_p| &= |\mathbf{r}_1 \times \mathbf{r}_2| \end{aligned}$$

which can be rewritten to obtain the expression given by Bertin and Smith:<sup>14</sup>

$$|\mathbf{r}_p| = \frac{|\mathbf{r}_1 \times \mathbf{r}_2|}{|\mathbf{r}_0|}$$

Collecting terms and making use of the vector identity provided in the sidebar, we obtain the Bertin and Smith statement of the Biot-Savart Law for a finite length vortex segment:

$$\mathbf{V}_p = \frac{1}{4} \frac{\mathbf{r}_1 \times \mathbf{r}_2}{|\mathbf{r}_1 \times \mathbf{r}_2|^2} \mathbf{r}_0 \left( \frac{\mathbf{r}_1}{|\mathbf{r}_1|} - \frac{\mathbf{r}_2}{|\mathbf{r}_2|} \right) \quad (6-48)$$

For a single infinite length horseshoe vortex we will use three segments, each using the formula given above. The nomenclature is given in the sketch below. The primary points are the

connecting points  $A$  and  $B$ . Between  $A$  and  $B$  we use a finite length vortex which is considered a “bound” vortex, and from  $A$  to infinity and  $B$  to infinity we define “trailing” vortices that are parallel to the  $x$ -axis.

The general expression for the velocity at a point  $x, y, z$  due to a horseshoe vortex at  $(x_{1n}, y_{1n}, z_{1n}), (x_{2n}, y_{2n}, z_{2n})$  with trailing vortices parallel to the  $x$ -axis is (from Bertin and Smith<sup>14</sup>):

$$\mathbf{V} = \mathbf{V}_{AB} + \mathbf{V}_A + \mathbf{V}_B \quad (6-49)$$

where the total velocity is the sum of the contributions from the three separate straight line vortex segments making up the horseshoe vortex, as shown in Fig. 6-11.

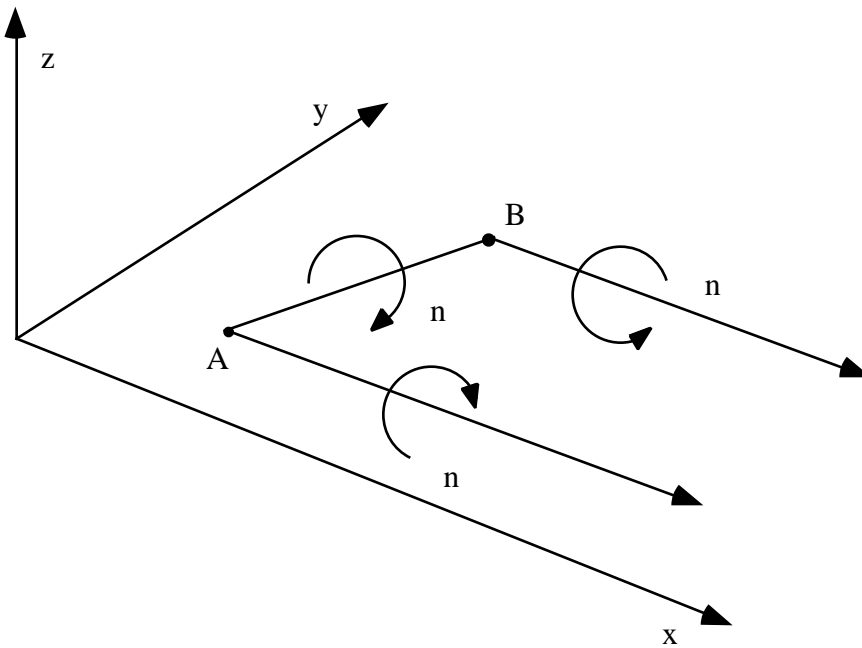


Figure 6-11. Definitions for notation used in induced velocity expressions.

The corner points of the vortex,  $A$  and  $B$ , are arbitrary, and are given by:

$$\begin{aligned} A &= A(x_{1n}, y_{1n}, z_{1n}) \\ B &= B(x_{2n}, y_{2n}, z_{2n}) \end{aligned} \quad (6-50)$$

We now write the expression for the velocity field at a general point in space  $(x, y, z)$  due to the horseshoe vortex system. At  $C(x, y, z)$  find the induced velocity due to each vortex segment. Start with  $AB$ , and use Fig. 6-12.

Now we define the vectors as:

$$\begin{aligned}
 \mathbf{r}_0 &= (x_{2n} - x_{1n})\mathbf{i} + (y_{2n} - y_{1n})\mathbf{j} + (z_{2n} - z_{1n})\mathbf{k} \\
 \mathbf{r}_1 &= (x - x_{1n})\mathbf{i} + (y - y_{1n})\mathbf{j} + (z - z_{1n})\mathbf{k} \\
 \mathbf{r}_2 &= (x - x_{2n})\mathbf{i} + (y - y_{2n})\mathbf{j} + (z - z_{2n})\mathbf{k}
 \end{aligned}
 \tag{6-51}$$

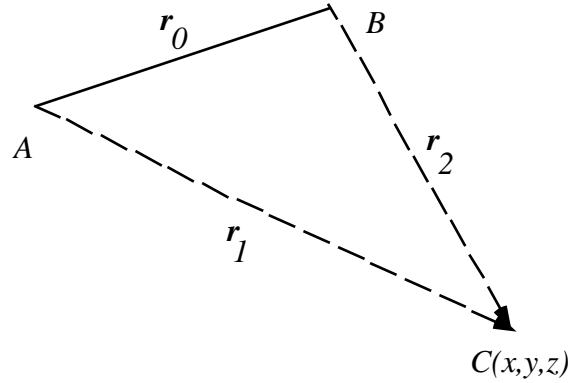


Figure 6-12. Velocity induced at Point C due to the vortex between A and B.

and we simply substitute into:

$$\mathbf{V}_C = \frac{1}{4} \frac{\mathbf{r}_1 \times \mathbf{r}_2}{|\mathbf{r}_1 \times \mathbf{r}_2|^2} \left( \mathbf{r}_0 \frac{\mathbf{r}_1}{|\mathbf{r}_1|} - \mathbf{r}_0 \frac{\mathbf{r}_2}{|\mathbf{r}_2|} \right)
 \tag{6-52}$$

Considering the bound vortex on AB first we obtain,

$$\mathbf{V}_{AB} = \frac{n}{4}
 \tag{6-53}$$

where  $\mathbf{r}_1$  and  $\mathbf{r}_2$  are lengthy expressions. By following the vector definitions, Eqn. (6-53) can be written in Cartesian coordinates. The vector  $\mathbf{V}_{AB}$  is:

$$\begin{aligned}
 &= \frac{\mathbf{r}_1 \times \mathbf{r}_2}{|\mathbf{r}_1 \times \mathbf{r}_2|^2} \\
 &\quad [(y - y_{1n})(z - z_{2n}) - (y - y_{2n})(z - z_{1n})]\mathbf{i} \\
 &\quad - [(x - x_{1n})(z - z_{2n}) - (x - x_{2n})(z - z_{1n})]\mathbf{j} \\
 &\quad + [(x - x_{1n})(y - y_{2n}) - (x - x_{2n})(y - y_{1n})]\mathbf{k} \\
 &= \frac{[(y - y_{1n})(z - z_{2n}) - (y - y_{2n})(z - z_{1n})]^2}{[(y - y_{1n})(z - z_{2n}) - (y - y_{2n})(z - z_{1n})]^2} \\
 &\quad + [(x - x_{1n})(z - z_{2n}) - (x - x_{2n})(z - z_{1n})]^2 \\
 &\quad + [(x - x_{1n})(y - y_{2n}) - (x - x_{2n})(y - y_{1n})]^2
 \end{aligned}
 \tag{6-54}$$

The scalar portion of the expression,  $\phi$ , is:

$$\begin{aligned}
 &= \mathbf{r}_o \frac{\mathbf{r}_1}{|\mathbf{r}_1|} - \mathbf{r}_o \frac{\mathbf{r}_2}{|\mathbf{r}_2|} \\
 &= \frac{[(x_{2n} - x_{1n})(x - x_{1n}) + (y_{2n} - y_{1n})(y - y_{1n}) + (z_{2n} - z_{1n})(z - z_{1n})]}{\sqrt{(x - x_{1n})^2 + (y - y_{1n})^2 + (z - z_{1n})^2}} \\
 &\quad - \frac{[(x_{2n} - x_{1n})(x - x_{2n}) + (y_{2n} - y_{1n})(y - y_{2n}) + (z_{2n} - z_{1n})(z - z_{2n})]}{\sqrt{(x - x_{2n})^2 + (y - y_{2n})^2 + (z - z_{2n})^2}}
 \end{aligned} \quad (6-55)$$

We find the contributions of the trailing vortex legs using the same formula, but redefining the points 1 and 2. Then, keeping the 1 and 2 notation, define a downstream point, “3” and let  $x_3$  go to infinity. Thus the trailing vortex legs are given by:

$$\mathbf{V}_A = \frac{n}{4} \frac{(z - z_{1n})\mathbf{j} + (y_{1n} - y)\mathbf{k}}{[(z - z_{1n})^2 + (y_{1n} - y)^2]} \left[ 1.0 + \frac{x - x_{1n}}{\sqrt{(x - x_{1n})^2 + (y - y_{1n})^2 + (z - z_{1n})^2}} \right] \quad (6-56)$$

and

$$\mathbf{V}_B = -\frac{n}{4} \frac{(z - z_{2n})\mathbf{j} + (y_{2n} - y)\mathbf{k}}{[(z - z_{2n})^2 + (y_{2n} - y)^2]} \left[ 1.0 + \frac{x - x_{2n}}{\sqrt{(x - x_{2n})^2 + (y - y_{2n})^2 + (z - z_{2n})^2}} \right] \quad (6-57)$$

Note that  $\mathbf{V}_m$  is contained linearly in each expression, so that the expression given above can be arranged much more compactly by using (6-49) with (6-52), (6-56), and (6-57) as:

$$\mathbf{V}_m = \mathbf{C}_{mn} \mathbf{V}_n \quad (6-58)$$

and  $\mathbf{C}_{mn}$  is an influence coefficient for the  $n^{\text{th}}$  horseshoe vortex effect at the location  $m$ , including all three segments.

Now that we can compute the induced velocity field of a horseshoe vortex, we need to decide where to place the horseshoe vortices to represent a lifting surface.

## 6.6 Selection of Control Point/Vortex Location

Since we are interested in using the horseshoe vortex defined above to represent a lifting surface, we need to examine exactly how this might be done. In particular: where do you locate the vortex, and where do you locate a control point to satisfy the surface boundary condition? Tradition has been to determine their locations by comparison with known results. In particular, we use two dimensional test cases, and then apply them directly to the three dimensional case.

An alternate distribution based on numerical properties of quadrature formulas has been derived by Lan. Section 6.11 will demonstrate the use of his vortex/control point locations in the inverse case, where the pressure is given, and the shape of the surface is sought.

*a) Simplest Approach: A Flat Plate*

Consider representing the flow over a flat plate airfoil by a single vortex and control point. Comparing with the known result from thin airfoil theory we determine the spacing between the vortex and control point which produces a lift identical with the thin airfoil theory value.

Consider the flat plate as sketched in Fig. 6-13.

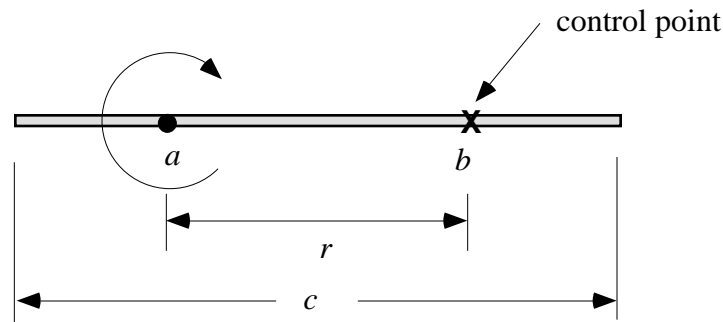


Figure 6-13. The notation for control point and vortex location analysis.

The velocity at the control point,  $cp$ , due to the point vortex is:

$$v_{cp} = -\frac{\Gamma}{2r} \quad (6-59)$$

The flow tangency condition was given above as:

$$\frac{v_{BC}}{V} = \frac{df_c}{dx} \quad (6-60)$$

and ignoring camber:

$$\frac{v_{BC}}{V} = - \quad (6-61)$$

or:

$$v_{BC} = - V \quad (6-62)$$

Now, we equate  $v_{BC}$  and  $v_{cp}$ :

$$-\frac{\Gamma}{2r} = - V \quad (6-63)$$

resulting in the expression for :

$$= \frac{1}{2} \frac{c}{rV} \cdot \quad (6-64)$$

To make use of this relation, recall the Kutta-Joukowski Theorem:

$$L = \rho V \Gamma \quad (6-65)$$

and the result from thin airfoil theory:

$$L = \frac{1}{2} \underbrace{\rho V^2}_{q} \underbrace{c}_{S_{ref}} \underbrace{C_L}_{2} \cdot \quad (6-66)$$

Equate the expressions for lift, Eqns. (6-65) and (6-66) and substitute for  $\Gamma$  using the expression in Eqn. (6-64) given above:

$$\begin{aligned} \rho V \Gamma &= \frac{1}{2} \rho V^2 c 2 \\ &= \frac{1}{2} \rho V^2 c 2 \frac{1}{2} \frac{c}{rV} \\ 1 &= \frac{1}{2} \frac{c}{r} \end{aligned} \quad (6-67)$$

and finally:

$$r = \frac{c}{2} \cdot \quad (6-68)$$

This defines the relation between the vortex placement and the control point in order for the single vortex model to reproduce the theoretical lift of an airfoil predicted by thin airfoil theory. Since the flat plate has constant (zero) camber everywhere, this case doesn't pin down placement (distance of the vortex from the leading edge) completely. Intuitively, the vortex should be located at the quarter-chord point since that is the location of the aerodynamic center of a thin flat plate airfoil. The next example is used to determine the placement of the vortex.

*b) Determine placement of the vortex using parabolic camber model.*

Rewrite the velocity at the control point due to the point vortex in a little more detail, where  $a$  denotes the location of the vortex, and  $b$  the location of the control point:

$$v_{cp} = -\frac{\Gamma}{2(a-b)} \quad (6-69)$$

and the boundary condition remains the same:

$$v_{BC} = V \frac{df_c}{dx} - v_{cp} \cdot \quad (6-70)$$

Equating the above expressions (and dividing by  $V$ ):

$$-\frac{1}{2(a-b)V} = \frac{df_c}{dx} \quad (6-71)$$

For parabolic camber,

$$f_c(x) = 4 \frac{x}{c} (c-x) \quad (6-72)$$

we have the slope,

$$\frac{df_c(x)}{dx} = 4 \left( 1 - 2 \frac{x}{c} \right) \quad (6-73)$$

so that:

$$-\frac{1}{2(a-b)V} = 4 \left( 1 - 2 \frac{x}{c} \right) \quad (6-74)$$

Now use the result from thin airfoil theory:

$$L = \frac{1}{2} V^2 c \alpha \left( 1 + 2 \frac{b}{c} \right)$$

and substitute for the lift from the Kutta-Joukowski theorem. We thus obtain an expression for the circulation of the vortex in terms of the angle of attack and camber:

$$\Gamma = V c \alpha \left( 1 + 2 \frac{b}{c} \right) \quad (6-75)$$

Substitute for  $\Gamma$  from (6-75) into (6-74), and satisfy the boundary condition at  $x = b$ :

$$-\frac{1}{2(b-a)V} = \frac{V c \alpha \left( 1 + 2 \frac{b}{c} \right)}{2(b-a)V} = 4 \left( 1 - 2 \frac{b}{c} \right)$$

or:

$$-\frac{1}{2} \frac{c}{b-a} \left( 1 + 2 \frac{b}{c} \right) = 4 \left( 1 - 2 \frac{b}{c} \right) \quad (6-76)$$

To be true for arbitrary  $\alpha$ , the coefficients must be equal:

$$\begin{aligned} -\frac{1}{2} \frac{c}{b-a} &= -1 \\ -\frac{c}{b-a} &= 4 \left( 1 - 2 \frac{b}{c} \right) \end{aligned} \quad (6-77)$$

and we solve for  $a$  and  $b$ . The first relation can be solved for  $(b-a)$ :

$$(b-a) = \frac{c}{2} \quad (6-78)$$

and we obtain the same results obtained above, validating our previous analysis ( $r = c/2$ ).

Now, rewrite the 2<sup>nd</sup> equation:

$$-c = 4 \left( 1 - 2 \frac{b}{c} \right) (b - a)$$

or:

$$-c = 4 \left( 1 - 2 \frac{b}{c} \right) \frac{c}{2} \quad (6-79)$$

and solve for  $b/c$ :

$$-1 = 2 \left( 1 - 2 \frac{b}{c} \right)$$

$$-\frac{1}{2} = 1 - 2 \frac{b}{c}$$

$$2 \frac{b}{c} = 1 + \frac{1}{2} = \frac{3}{2}$$

$$\frac{b}{c} = \frac{1}{2} \frac{3}{2} = \frac{3}{4}, \quad (6-80)$$

and use this to solve for  $a/c$  starting with Eqn. (6-78) :

$$(b - a) = \frac{c}{2}$$

or:

$$\frac{b}{c} - \frac{a}{c} = \frac{1}{2} \quad (6-81)$$

and:

$$\frac{a}{c} = \frac{b}{c} - \frac{1}{2} = \frac{3}{4} - \frac{1}{2}.$$

Finally:

$$\frac{a}{c} = \frac{1}{4}. \quad (6-82)$$

Thus the vortex is located at the 1/4 chord point, and the control point is located at the 3/4 chord point. Naturally, this is known as the “1/4 - 3/4 rule.” It’s not a theoretical law, simply a placement that works well and has become a rule of thumb. It was discovered by Italian Pistolesi. Mathematical derivations of more precise vortex/control point locations are available (see Lan<sup>6</sup>), but the 1/4 - 3/4 rule is widely used, and has proven to be sufficiently accurate in practice.

To examine the use of these ideas we present a two-dimensional example. The airfoil is divided into a number of equal size panels. Each panel has a vortex at the quarter chord point and the non-penetration condition is satisfied at the three-quarter chord point. We use the example to illustrate the accuracy of the classical thin airfoil theory formulation. In Fig. 6-14, we compare the results obtained for a 5% circular arc camber.\* Three solutions are presented. The linear theory curve uses classical thin airfoil theory with results obtained satisfying the boundary condition on the mean surface. This is compared with numerical results for the case where the boundary condition is applied exactly on the camber line, and the result obtained applying the boundary condition using the approximate method described above. The difference between placing the vortex on the actual camber surface and satisfying the boundary condition on the actual surface, and the more approximate traditional approach of locating the vortex and control point on the mean surface is extremely small.

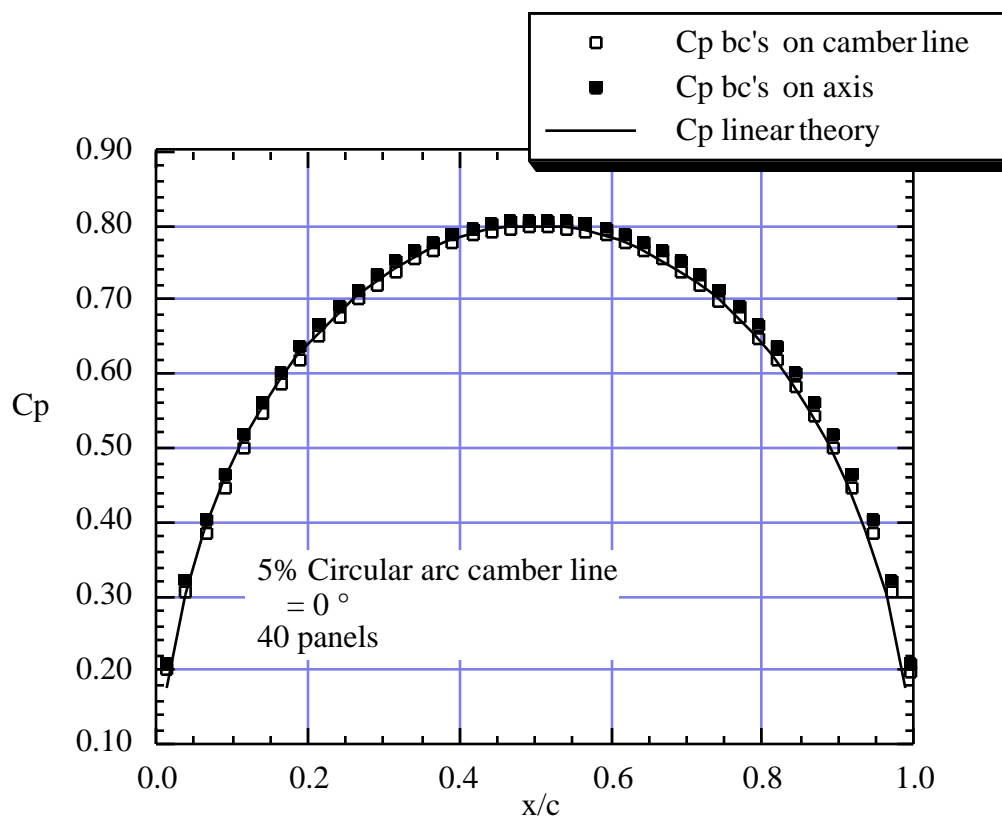


Figure 6-14. Comparison in 2D of the 1/4-3/4 rule for vortex-control point locations with linear theory, and including a comparison between placing the vortex and control point on the camber line or on the axis.

\* A relatively large camber for a practical airfoil, the NACA 4412 example we used in Chapter 4 was an extreme case, and it has 4% camber.

## 6.7 The Classical Vortex Lattice Method

There are many different vortex lattice schemes. In this section we describe the “classical” implementation. Knowing that vortices can represent lift from our airfoil analysis, and that one approach is to place the vortex and then satisfy the boundary condition using the “1/4 - 3/4 rule,” we proceed as follows:

1. Divide the planform up into a lattice of quadrilateral panels, and put a horseshoe vortex on each panel.
2. Place the bound vortex of the horseshoe vortex on the 1/4 chord element line of each panel.
3. Place the control point on the 3/4 chord point of each panel at the midpoint in the spanwise direction (sometimes the lateral panel centroid location is used) .
4. Assume a flat wake in the usual classical method.
5. Determine the strengths of each  $\Gamma_n$  required to satisfy the boundary conditions by solving a system of linear equations. The implementation is shown schematically in Fig. 6-15.

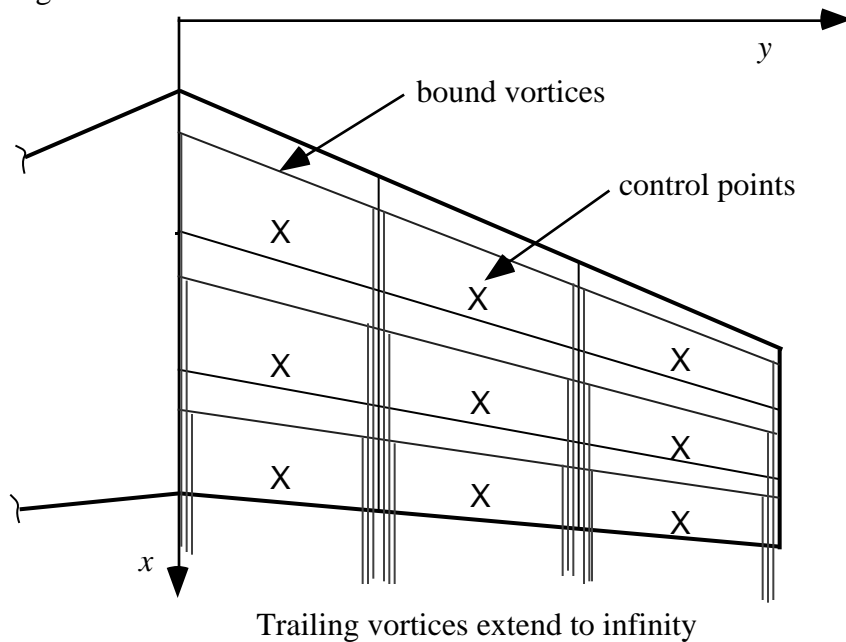


Figure 6-15. The horseshoe vortex layout for the classical vortex lattice method.

Note that the lift is on the bound vortices. To understand why, consider the vector statement of the Kutta-Joukowski Theorem,  $\mathbf{F} = \mathbf{V} \times \boldsymbol{\Gamma}$ . Assuming the freestream velocity is the primary contributor to the velocity, the trailing vortices are parallel to the velocity vector and hence the force on the trailing vortices are zero. More accurate methods find the wake deformation required to eliminate the force in the presence of the complete induced flowfield.

Next, we derive the mathematical statement of the classical vortex lattice method described above. First, recall that the velocity induced by a single horseshoe vortex is

$$\mathbf{V}_m = \mathbf{C}_{m,n} \mathbf{n} \cdot \quad (6-60)$$

This is the velocity induced at the point  $m$  due to the  $n^{th}$  horseshoe vortex, where  $\mathbf{C}_{m,n}$  is a vector, and the components are given by Equations 6-54, 6-58 and 6-59.

The total induced velocity at  $m$  due to the  $2N$  vortices ( $N$  on each side of the planform) is:

$$\mathbf{V}_{m_{ind}} = u_{m_{ind}} \mathbf{i} + v_{m_{ind}} \mathbf{j} + w_{m_{ind}} \mathbf{k} = \sum_{n=1}^{2N} \mathbf{C}_{m,n} \mathbf{n} \cdot \quad (6-83)$$

The solution requires the satisfaction of the boundary conditions for the total velocity, which is the sum of the induced and freestream velocity. The freestream velocity is (introducing the possibility of considering vehicles at combined angle of attack and sideslip):

$$\mathbf{V} = V \cos \alpha \cos \beta \mathbf{i} - V \sin \alpha \mathbf{j} + V \sin \alpha \cos \beta \mathbf{k} \quad (6-84)$$

so that the total velocity at point  $m$  is:

$$\mathbf{V}_m = (V \cos \alpha \cos \beta + u_{m_{ind}}) \mathbf{i} + (-V \sin \alpha + v_{m_{ind}}) \mathbf{j} + (V \sin \alpha \cos \beta + w_{m_{ind}}) \mathbf{k} \cdot \quad (6-85)$$

The values of the unknown circulations,  $\Gamma_n$ , are found by satisfying the non-penetration boundary condition at all the control points simultaneously. For steady flow this is

$$\mathbf{V} \cdot \mathbf{n} = 0 \quad (6-1)$$

where the surface is described by

$$F(x, y, z) = 0. \quad (6-86)$$

Equation (6-1) can then be written:

$$\mathbf{V} \cdot \frac{\nabla F}{|\nabla F|} = \mathbf{V} \cdot \nabla F = 0. \quad (6-87)$$

This equation provides freedom to express the surface in a number of forms. The most general form is obtained by substituting Eqn. (6-85) into Eqn. (6-87) using Eqn. (6-83). This can be written as:

$$\left[ (V \cos \alpha \cos \beta + u_{m_{ind}}) \mathbf{i} + (-V \sin \alpha + v_{m_{ind}}) \mathbf{j} + (V \sin \alpha \cos \beta + w_{m_{ind}}) \mathbf{k} \right] \cdot \left[ \frac{F}{x} \mathbf{i} + \frac{F}{y} \mathbf{j} + \frac{F}{z} \mathbf{k} \right] = 0 \quad (6-88)$$

or:

$$\begin{aligned}
(V \cos \alpha \cos \beta + \sum_{n=1}^{2N} C_{m,n_i} n) \mathbf{i} + (-V \sin \alpha + \sum_{n=1}^{2N} C_{m,n_j} n) \mathbf{j} + (V \sin \alpha \cos \beta + \sum_{n=1}^{2N} C_{m,n_k} n) \mathbf{k} \\
\frac{F}{x} \mathbf{i} + \frac{F}{y} \mathbf{j} + \frac{F}{z} \mathbf{k} = 0
\end{aligned} \tag{6-89}$$

Carrying out the dot product operation and collecting terms:

$$\begin{aligned}
\frac{F}{x} (V \cos \alpha \cos \beta + \sum_{n=1}^{2N} C_{m,n_i} n) + \frac{F}{y} (-V \sin \alpha + \sum_{n=1}^{2N} C_{m,n_j} n) + \\
\frac{F}{z} (V \sin \alpha \cos \beta + \sum_{n=1}^{2N} C_{m,n_k} n) = 0.
\end{aligned} \tag{6-90}$$

Recall that Eqn. (6-90) is applied to the boundary condition at point  $m$ . Next, we collect terms to clearly identify the expression for the circulation. The resulting expression defines a system of equations for all the panels, and is the system of linear algebraic equations that is used to solve for the unknown values of the circulation distribution. The result is:

$$\sum_{n=1}^{2N} \left( \frac{F}{x} C_{m,n_i} + \frac{F}{y} C_{m,n_j} + \frac{F}{z} C_{m,n_k} \right) n = -V \left( \cos \alpha \cos \beta \frac{F}{x} - \sin \alpha \frac{F}{y} + \sin \alpha \cos \beta \frac{F}{z} \right) \tag{6-91}$$

$m = 1, \dots, 2N$

This is the general equation used to solve for the values of the circulation. It is arbitrary, containing effects of both angle of attack and sideslip (if the vehicle is at sideslip the trailing vortex system should be yawed to align it with the freestream).

If the surface is primarily in the  $x$ - $y$  plane and the sideslip is zero, we can write a simpler form. In this case the natural description of the surface is

$$z = f(x, y) \tag{6-92}$$

and

$$F(x, y, z) = z - f(x, y) = 0. \tag{6-93}$$

The gradient of  $F$  becomes

$$\frac{F}{x} = -\frac{f}{x}, \quad \frac{F}{y} = -\frac{f}{y}, \quad \frac{F}{z} = 1. \tag{6-94}$$

Substituting into the statement of the boundary condition, Eqn. (6-91), we obtain:

$$\sum_{n=1}^{2N} \left( C_{m,n_k} - \frac{f}{x} C_{m,n_i} - \frac{f}{y} C_{m,n_j} \right) n = V \left( \cos \alpha \frac{f}{x} - \sin \alpha \right), \quad m = 1, \dots, 2N. \tag{6-95}$$

This equation provides the solution for the vortex lattice problem.

Note that if an essentially vertical surface is of interest, the form of  $F$  is more naturally

$$F = y - g(x, z),$$

and this should be used to work out the boundary condition in a similar fashion.

To illustrate the usual method, consider the simple planar surface case, where there is no dihedral. Furthermore, recalling the example in the last section and the analysis at the beginning of the chapter, the thin airfoil theory boundary conditions can be applied on the mean surface, and not the actual camber surface. We also use the small angle approximations. Under these circumstances, Eq. (6-95) becomes:

$$w_m = \sum_{n=1}^{2N} C_{m,n} \frac{1}{V} = \frac{df_c}{dx} - \alpha_m \quad (6-96)$$

Thus we have the following equation which satisfies the boundary conditions and can be used to relate the circulation distribution and the wing camber and angle of attack:

$$\sum_{n=1}^{2N} C_{m,n} \frac{1}{V} = \frac{df_c}{dx} - \alpha_m \quad m = 1, \dots, 2N \quad (6-97)$$

Equation (6-97) contains two cases:

1. *The Analysis Problem.* Given camber slopes and  $\alpha$ , solve for the circulation strengths,  $(C_{m,n}/V)$  [a system of  $2N$  simultaneous linear equations].
- or
2. *The Design Problem.* Given  $(C_{m,n}/V)$ , which corresponds to a specified surface loading, we want to find the camber and  $\alpha$  required to generate this loading (only requires simple algebra, no system of equations must be solved).

Notice that the way  $df_c/dx$  and  $\alpha$  are combined illustrates that the division between camber, angle of attack and wing twist is arbitrary (twist can be considered a separate part of the camber distribution, and is useful for wing design). However, care must be taken in keeping the bookkeeping straight.

One reduction in the size of the problem is available in many cases. If the geometry is symmetrical and the camber and twist are also symmetrical, then  $C_{m,n}$  is the same on each side of the planform (but *not* the influence coefficient). Therefore, we only need to solve for  $N$   $C_{m,n}$ 's, not  $2N$  (this is true also if ground effects are desired, see Katz and Plotkin<sup>11</sup>). The system of equations for this case becomes:

$$\sum_{n=1}^N C_{m,n_{\text{left}}} + C_{m,n_{\text{right}}} \frac{1}{V} = \frac{df_c}{dx} - \alpha_m \quad m = 1, \dots, N \quad (6-98)$$

This is easy. Why not just program it up ourselves? You can, but most of the work is:

- A. Automatic layout of panels for arbitrary geometry. As an example, when considering multiple lifting surfaces, the horseshoe vortices on each surface must “line up”. The downstream leg of a horseshoe vortex cannot pass through the control point of another panel.
- and
- B. Converting  $n$  to the aerodynamics values of interest,  $C_L$ ,  $C_m$ , *etc.*, and the spanload, is tedious for arbitrary configurations.

Nevertheless, many people (including previous students in the Applied Computational Aerodynamics class) have written **vlm** codes. The method is widely used in industry and government for aerodynamic estimates for conceptual and preliminary design predictions. The method provides good insight into the aerodynamics of wings, including interactions between lifting surfaces.

Typical analysis uses (in a design environment) include

- Predicting the configuration neutral point during initial configuration layout, and studying the effects of wing placement and canard and/or tail size and location.
- Finding the induced drag,  $C_{Di}$ , from the spanload in conjunction with farfield methods.
- With care, estimating control and device deflection effectiveness (estimates where viscous effects may be important require calibration. Some examples are shown in the next section. For example, take 60% of the inviscid value to account for viscous losses, and also realize that a deflection of  $\delta = 20 - 25^\circ$  is about the maximum useful device deflection in practice).
- Investigating the aerodynamics of interacting surfaces.
- Finding the lift curve slope,  $C_L$ , approach angle of attack, *etc.*

Typical design applications include:

- Initial estimates of twist to obtain a desired spanload, or root bending moment.
- Starting point for finding a camber distribution in purely subsonic cases.

Before examining how well the method works, two special cases require comments. The first case arises when a control point is in line with the projection of one of the finite length vortex segments. This problem occurs when the projection of a swept bound vortex segment from one side of the wing intersects a control point on the other side. This happens frequently. The velocity induced by this vortex is zero, but the equation as usually written degenerates into a singular form, with the denominator going to zero. Thus a special form should be used. In practice, when this happens the contribution can be set to zero without invoking the special form. Figure 6-16 shows how this happens. Using the Warren 12 planform and 36 vortices on each side of the wing, we see that the projection of the line of bound vortices on the last row of the left hand side of the planform has a projection that intersects one of the control points on the right hand side.

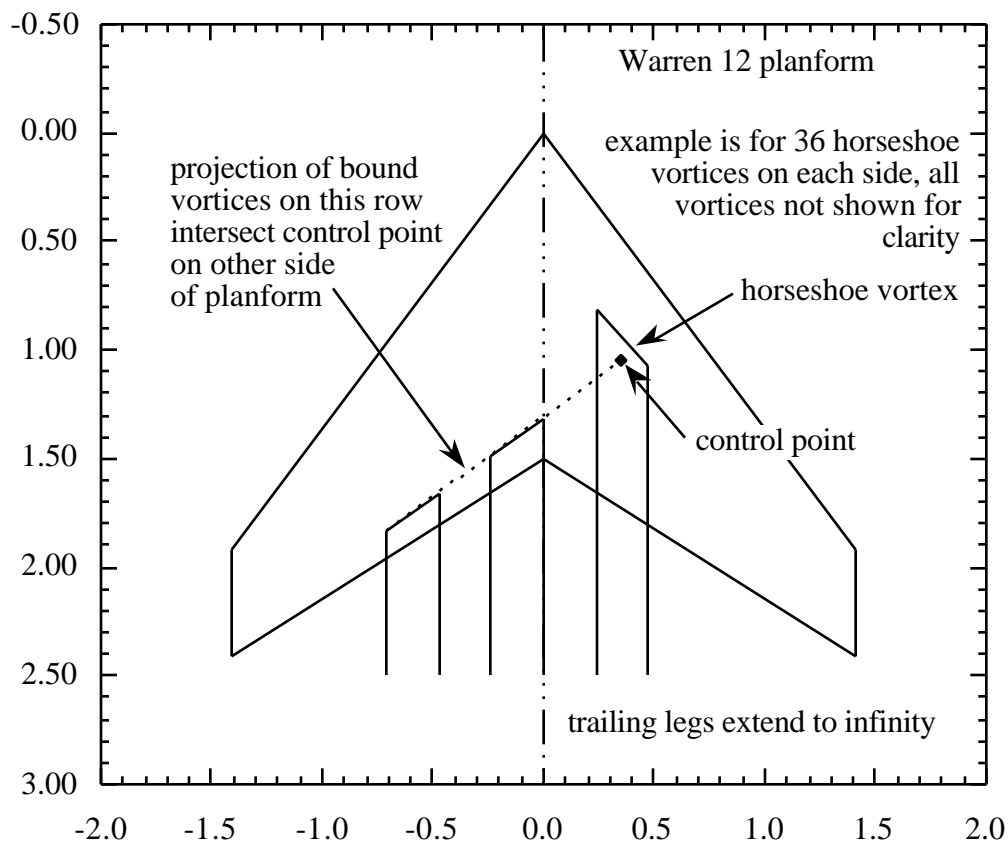


Figure 6-16. Example of case requiring special treatment, the intersection of the projection of a vortex with a control point.

A model problem illustrating this can be constructed for a simple finite length vortex segment. The velocity induced by this vortex is shown in Fig. 6-17. When the vortex is approached directly,  $x/l = 0.5$ , the velocity is singular for  $h = 0$ . However, as soon as you approach the axis ( $h = 0$ ) off the end of the segment ( $x/l > 1.0$ ) the induced velocity is zero. This illustrates why you can set the induced velocity to zero when this happens.

This second case that needs to be discussed arises when two or more planforms are used with this method. This is one of the most powerful applications of the vortex lattice method. However, care must be taken to make sure that the trailing vortices from the first surface do not intersect the control points on the second surface. In this case the induced velocity is in fact infinite, and the method breaks down. Usually this problem is solved by using the same spanwise distribution of horseshoe vortices on each surface. This aligns the vortex the legs, and the control points are well removed from the trailing vortices of the forward surfaces.

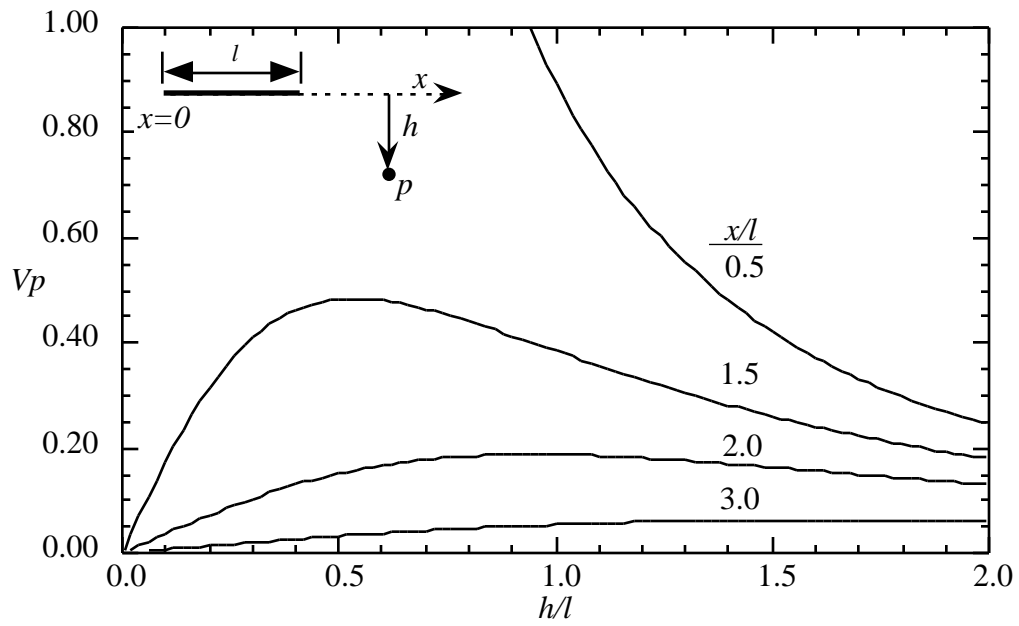


Figure 6-17. Velocity induced by finite straight line section of a vortex.

## 6.8 Examples of the Use and Accuracy of the vlm Method

How well does the method work? In this section we describe how the method is normally applied, and present some example results obtained using it. More examples and a discussion of the aerodynamics of wings and multiple lifting surfaces are given in Section 6.10.

The vortex lattice layout is clear for most wings and wing-tail or wing-canard configurations. The method can be used for wing-body cases by simply specifying the projected planform of the entire configuration as a flat lifting surface made up of a number of straight line segments. The exact origin of this somewhat surprising approach is unknown. The success of this approach is illustrated in examples given below.

To get good, consistent and reliable results some simple rules for panel layout should be followed. This requires that a few common rules of thumb be used in selecting the planform break points: i) the number of line segments should be minimized, ii) breakpoints should line up streamwise on front and rear portions of each planform, and should line up between planforms, iii) streamwise tips should be used, iv) small spanwise distances should be avoided by making edges streamwise if they are actually very highly swept, and v) trailing vortices from forward surfaces cannot hit the control point of an aft surface. Figure 6-18 illustrates these requirements.

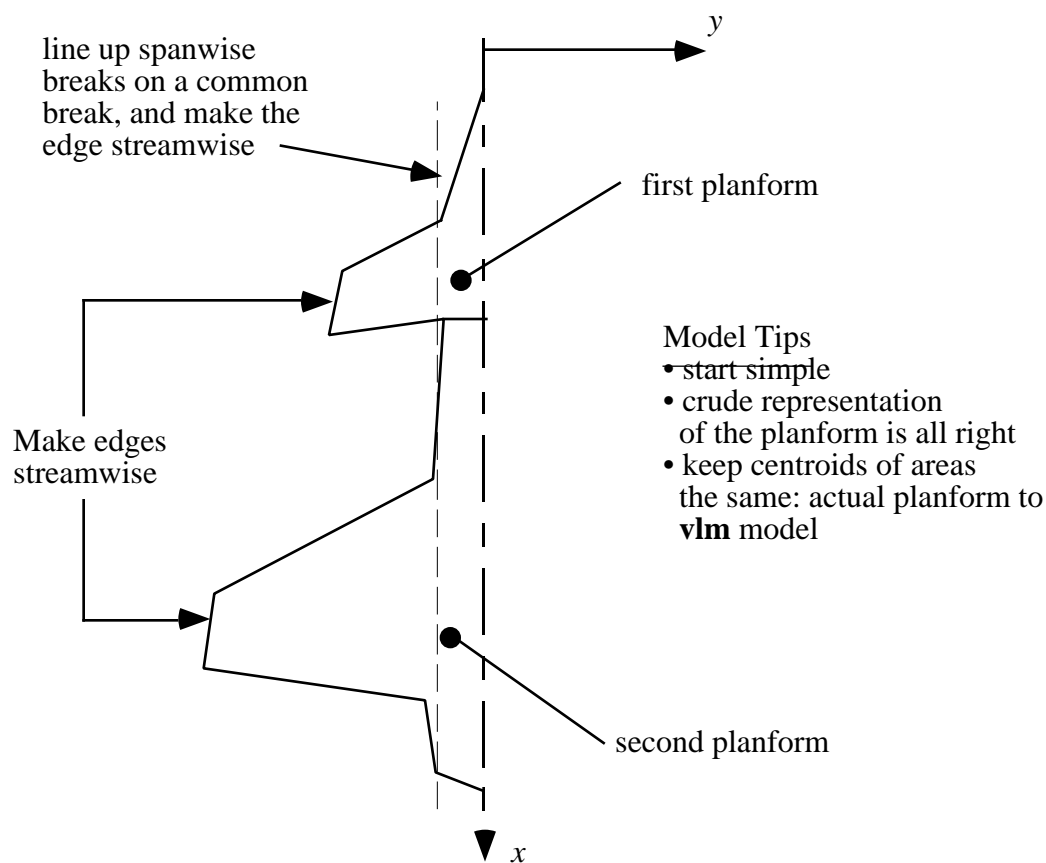


Figure 6-18. Example of a **vlm** model of an aircraft configuration. Note that one side of a symmetrical planform is shown.

Examples from three reports have been selected to illustrate the types of results that can be expected from vortex lattice methods. They illustrate the wide range of uses for the vlm method.

*Aircraft configurations examined by John Koegler<sup>15</sup>*

As part of a study on control system design methods, John Koegler at McDonnell Aircraft Company studied the prediction accuracy of several methods for fighter airplanes. In addition to the vortex lattice method, he also used the PAN AIR and Woodward II panel methods (see Chapter 4 for details of the panel methods). He compared his predictions with the three-surface F-15, which became known as the STOL/Maneuver demonstrator, and the F-18. These configurations are illustrated in Fig. 6-19.

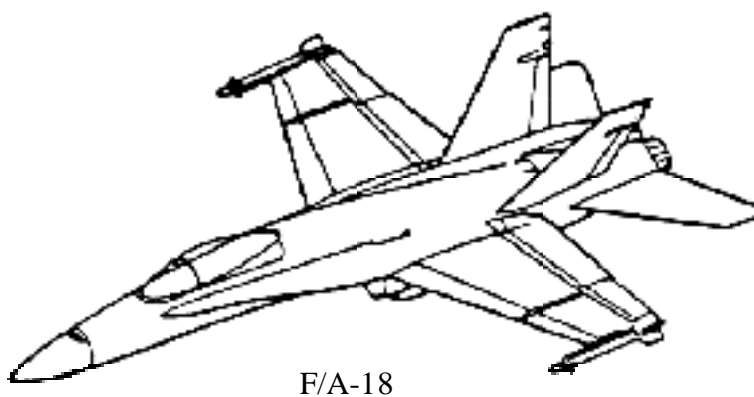
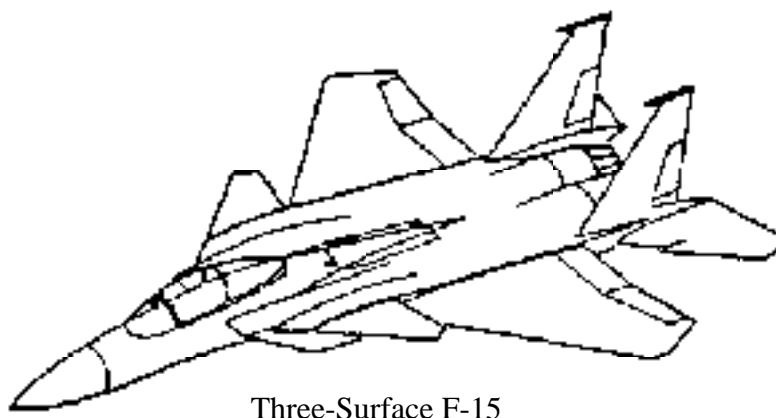


Figure 6-19. Configurations used by McDonnell Aircraft to study **vlm** method accuracy (Reference 15).

Considering the F-15 STOL/Maneuver demonstrator first, the basic panel layout is given in Figure 6-20. This shows how the aircraft was modeled as a flat planform, and the corner points of the projected configuration were used to represent the shape in the vortex lattice method and the panel methods. Note that in this case the rake of the wingtip was included in the computational model. In this study the panel methods were also used in a purely planar surface mode. In the vortex lattice model the configuration was divided into three separate planforms, with divisions at the wing root leading and trailing edges. On this configuration each surface was at a different height and, after some experimentation, the vertical distribution of surfaces shown in Figure 6-21 was found to provide the best agreement with wind tunnel data.

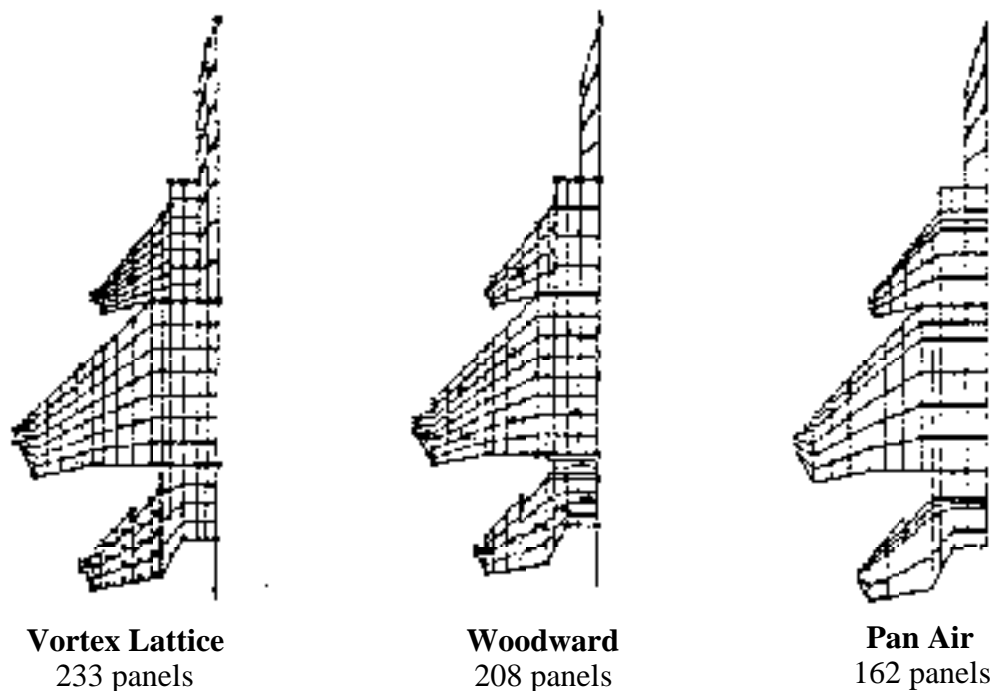


Figure 6-20. Panel models used for the three-surface F-15 (Ref.15).

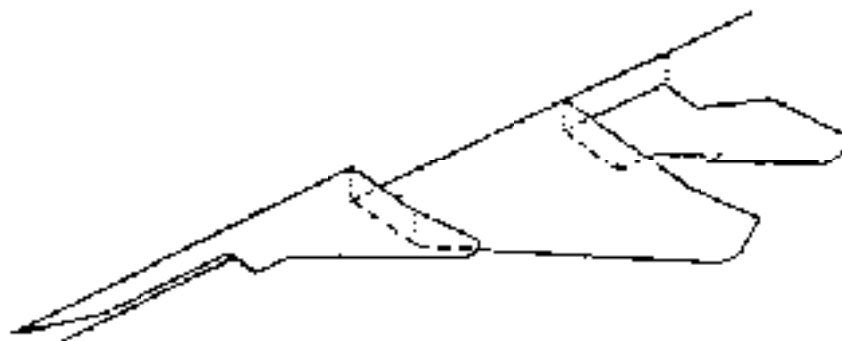


Figure 6-21. Canard and horizontal tail height representation (Ref. 15).

The results from these models are compared with wind tunnel data in Table 6-1. The vortex lattice method is seen to produce excellent agreement with the data for the neutral point location, and lift and moment curve slopes at Mach 0.2.

Subsonic Mach number effects are simulated in **vlm** methods by transforming the Prandtl-Glauert equation which describes the linearized subsonic flow to Laplace's Equation using the Göthert transformation. However, this is only approximately correct and the agreement with wind tunnel data is not as good at the transonic Mach number of 0.8. Nevertheless, the **vlm** method is as good as PAN AIR used in this manner. The **vlm** method is not applicable at supersonic speeds. The wind tunnel data shows the shift in the neutral point between subsonic and supersonic flow. The Woodward method, as applied here, over predicted the shift with Mach number. Note that the three-surface configuration is neutral to slightly unstable subsonically, and becomes stable at supersonic speeds.

Figure 6-22 provides an example of the use of the **vlm** method to study the effects of moving the canard. Here, the wind tunnel test result is used to validate the method and to provide an "anchor" for the numerical study (it would have been useful to have to have an experimental point at -15 inches). This is typical of the use of the **vlm** method in aircraft design. When the canard is above the wing the neutral point is essentially independent of the canard height. However when the canard is below the wing the neutral point varies rapidly with canard height.

| Table 6-1<br>Three-Surface F-15 Longitudinal Derivatives |                |                          |                  |                  |
|----------------------------------------------------------|----------------|--------------------------|------------------|------------------|
| Data Source                                              |                | Neutral Point<br>(% mac) | $C_m$<br>(1/deg) | $C_L$<br>(1/deg) |
| M = 0.2                                                  | Wind Tunnel    | 15.70                    | .00623           | .0670            |
|                                                          | Vortex Lattice | 15.42                    | .00638           | .0666            |
|                                                          | Woodward       | 14.18                    | .00722           | .0667            |
|                                                          | Pan Air        | 15.50                    | .00627           | .0660            |
| M = 0.8                                                  | Wind Tunnel    | 17.70                    | .00584           | .0800            |
|                                                          | Vortex Lattice | 16.76                    | .00618           | .0750            |
|                                                          | Pan Air        | 15.30                    | .00684           | .0705            |
| M = 1.6                                                  | Wind Tunnel    | 40.80                    | -.01040          | .0660            |
|                                                          | Woodward       | 48.39                    | -.01636          | .0700            |

from reference 15, Appendix by John Koegler

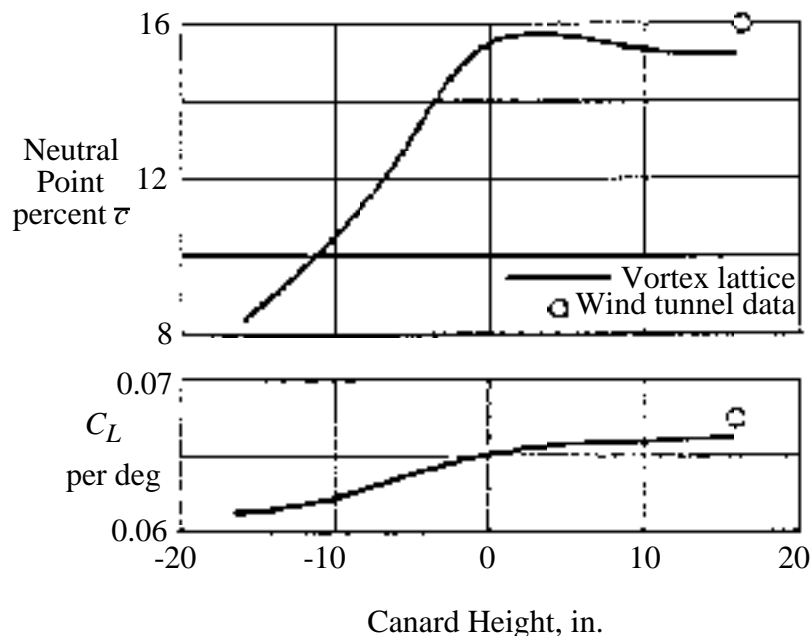


Figure 6-22. Effect of canard height variation on three-surface F-15 characteristics (Ref. 15).

Control effectiveness is also of interest in conceptual and preliminary design, and the **vlm** method can be used to provide estimates. Figure 6-23 provides an apparently accurate example of this capability for F-15 horizontal tail effectiveness. Both  $C_{L h}$  and  $C_{m h}$  are presented. The **vlm** estimate is within 10% accuracy at both Mach .2 and .8. However, the F-15 has an all moving horizontal tail to provide sufficient control power under both maneuvering and supersonic flight conditions. Thus the tail effectiveness presented here is effectively a measure of the accuracy of the prediction of wing lift and moment change with angle of attack in a non-uniform flowfield, rather than the effectiveness of a flap-type control surface. A flapped device such as a horizontal stabilizer and elevator combination will have significantly larger viscous effects, and the inviscid estimate from a vortex lattice or panel method (or any inviscid method) will overpredict the control effectiveness. This is shown next for an aileron.

The aileron effectiveness for the F-15 presented in Fig. 6-24 is more representative of classical elevator or flap effectiveness correlation between **vlm** estimates and experimental data. This figure presents the roll due to aileron deflection. In this case the device deflection is subject to significant viscous effects, and the figure shows that only a portion of the effectiveness predicted by the **vlm** method is realized in the actual data. The **vlm** method, or *any* method, should always be calibrated with experimental data close to the cases of interest to provide an indication of the agreement between theory and experiment. In this case the actual results are found to be about 60% of the inviscid prediction at low speed.

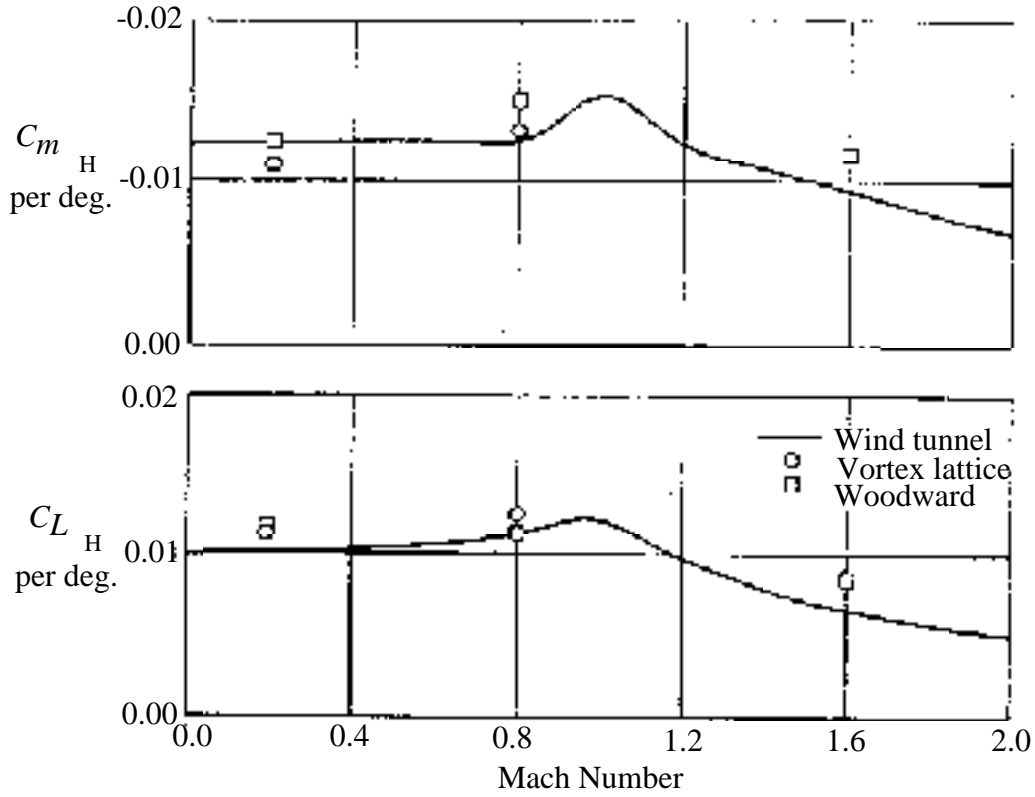


Figure 6-23. F-15 horizontal tail effectiveness (Ref. 15).

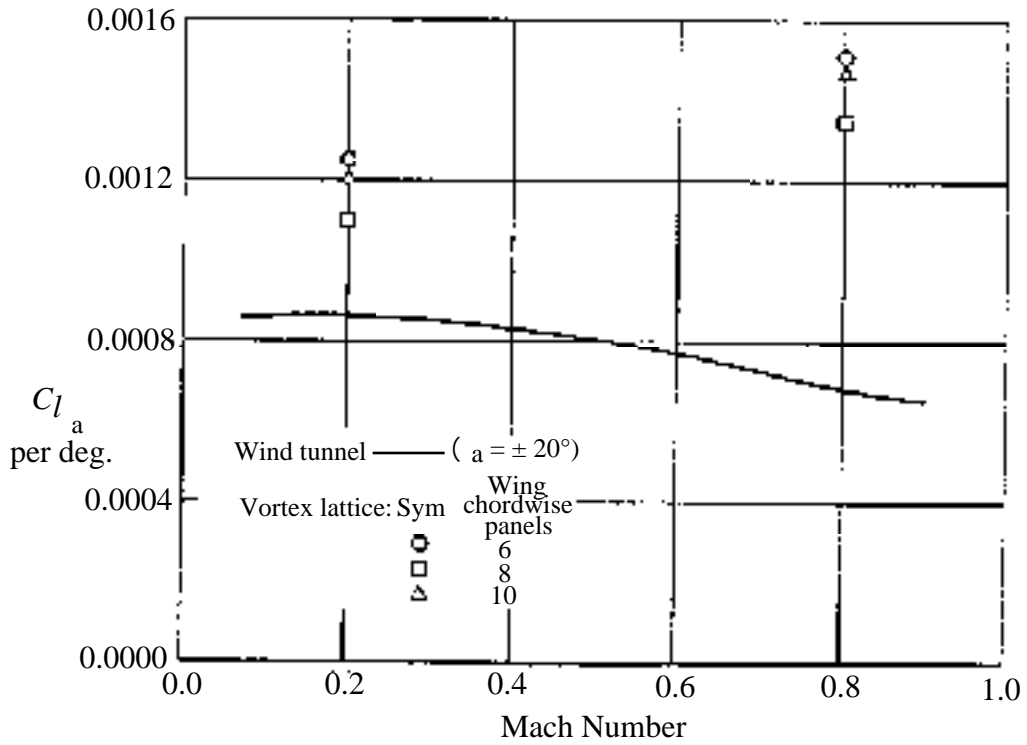


Figure 6-24. F-15 aileron effectiveness (Ref. 15).

The F/A-18 was also considered by Kogler. In this case the contributions to the longitudinal derivatives by the wing-tip missiles and the vertical tail were investigated (the vertical tails are canted outward on the F/A-18). The panel scheme used to estimate the effects of the wing-tip missile and launcher is shown in Figure 6-25. The results are given in Table 6-2. Here the computational increments are compared with the wind tunnel increments. The **vlm** method over predicts the effect of the wing-tip missiles, and under predicts the effects of the contribution of the vertical tail to longitudinal characteristics due to the cant of the tail (recall that on the F/A-18 the rudders are canted inward at takeoff to generate an additional nose up pitching moment) .

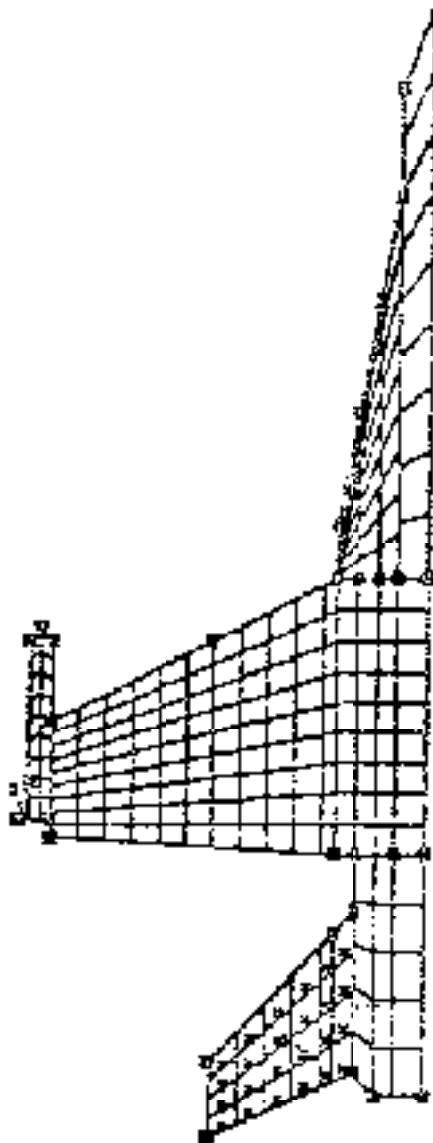
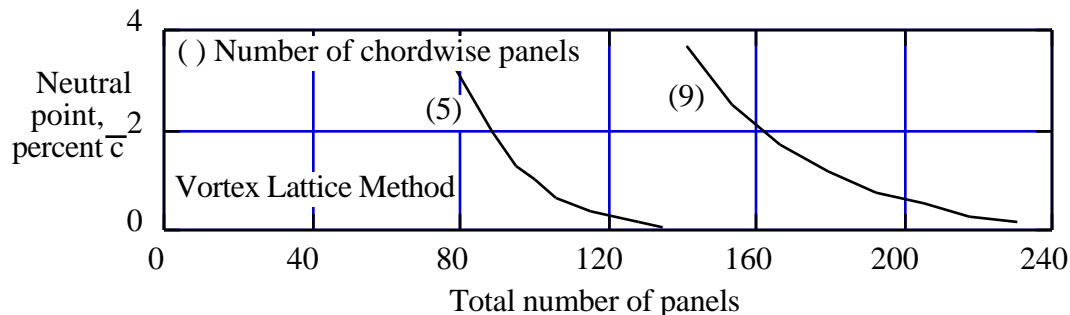


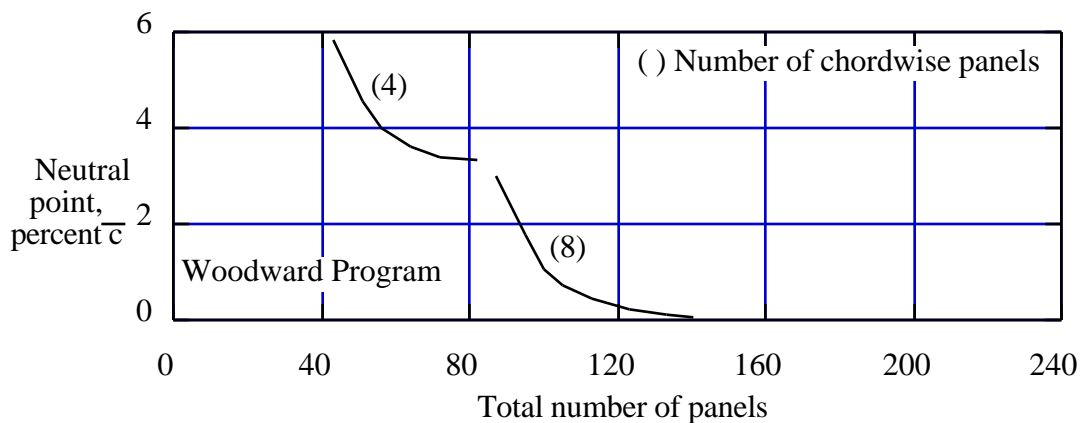
Figure 6-25. F/A-18 panel scheme with wing-tip missile and launcher (Ref. 15).

| <b>Table 6-2</b><br>F/A-18 Increments Due To Adding Wing-Tip Missiles and Launchers, and Vertical Tails |                |             |                       |               |               |
|---------------------------------------------------------------------------------------------------------|----------------|-------------|-----------------------|---------------|---------------|
|                                                                                                         |                | Mach Number | Neutral Point (% mac) | $C_M$ (1/deg) | $C_L$ (1/deg) |
| Wing Tip Missiles and Launchers                                                                         | Wind Tunnel    | 0.2         | 1.10                  | -0.00077      | 0.0020        |
|                                                                                                         | "              | 0.8         | 1.50                  | -0.00141      | 0.0030        |
|                                                                                                         | "              | 1.6         | -1.60                 | 0.00148       | 0.0030        |
|                                                                                                         | Vortex Lattice | 0.2         | 1.48                  | -0.00121      | 0.0056        |
|                                                                                                         | "              | 0.8         | 2.11                  | -0.00198      | 0.0082        |
|                                                                                                         | Woodward       | 0.2         | 1.52                  | -0.00132      | 0.0053        |
|                                                                                                         | "              | 0.8         | 1.77                  | -0.00180      | 0.0079        |
|                                                                                                         | "              | 1.6         | -0.17                 | 0.00074       | 0.0022        |
| Vertical Tails                                                                                          | Wind Tunnel    | 0.2         | 1.50                  | -0.00110      | 0.0050        |
|                                                                                                         | "              | 0.8         | 2.00                  | -0.00202      | 0.0080        |
|                                                                                                         | Vortex Lattice | 0.2         | 1.11                  | -0.00080      | 0.0022        |
|                                                                                                         | "              | 0.8         | 1.32                  | -0.00108      | 0.0026        |
| from refernce 15, Appendix by John Koegler                                                              |                |             |                       |               |               |

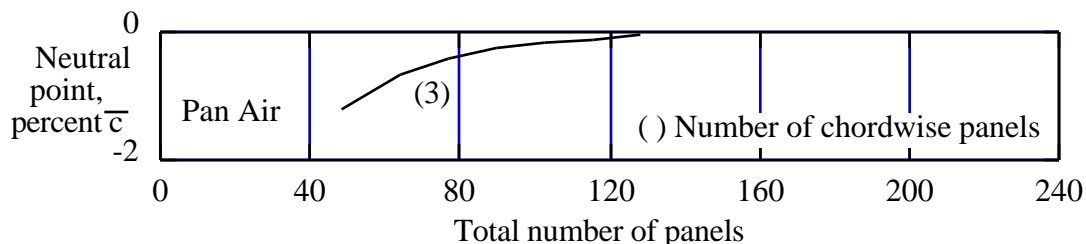
Finally, the effects of the number of panels and the way they are distributed is presented in Figure 6-26. In this case the **vlm** method is seen to take between 130 to 220 panels to produce converged results. For the vortex lattice method it appears important to use a large number of spanwise rows, and a relatively small number of chordwise panels (5 or 6 appear to be enough).



a) vortex lattice sensitivity to number of panels



b) Woodward program sensitivity to number of panels



c) Pan Air program sensitivity to number of panels

Figure 6-26. F/A-18 panel convergence study (Ref. 15).

Although this study has been presented last in this section, a study like this should be conducted before making a large number of configuration parametric studies. Depending on the relative span to length ratio the paneling requirements may vary. The study showed that from about 120 to 240 panels are required to obtain converged results. The vortex lattice methods obtains the best results when many spanwise stations are used, together with a relatively small number of chordwise panels. In that case about 140 panels provided converged results.

*Slender lifting body results from Jim Pittman*<sup>16</sup>

To illustrate the capability of the vortex lattice method for bodies that are more fuselage-like than wing-like, we present the lifting body comparison of the experimental and **vlm** results published by Jim Pittman of NASA Langley. Figure 6-27 shows the configuration used. Figure 6-28 provides the results of the vortex lattice method compared with the experimental data. In this case the camber shape was modeled by specifying camber slopes on the mean surface. The model used 138 vortex panels. The bars at several angles of attack illustrate the range of predictions obtained with different panel arrangements. For highly swept wings, leading edge vortex flow effects are included, as we will describe in Section 6.12. The program **VLMpc** available for this course contains the option of using the leading edge suction analogy to model these effects. Remarkably good agreement with the force and moment data is demonstrated in Fig. 6-28. The nonlinear variation of lift and moment with angle of attack arises due to the inclusion of the vortex lift effects. The agreement between data and computation breaks down at higher angles of attack because the details of the distribution of vortex flow separation are not provided by the leading edge suction analogy. The drag prediction is also very good. The experimental drag is adjusted by removing the zero lift drag, which contains the drag due to friction and separation. The resulting drag due to lift is compared with the **vlm** estimates. The comparisons are good primarily because this planform is achieving, essentially, no leading edge suction, and hence the drag is simply  $C_D = C_L \tan \alpha$ .

copyrighted figure from the AIAA *Journal of Aircraft*

Figure 6-27. Highly swept lifting body type hypersonic concept (Ref. 16).

copyrighted figure from the AIAA *Journal of Aircraft*

Figure 6-28. Comparison of  $C_L$ ,  $C_m$ , and  $C_D$  predictions with data (Ref. 16).

*Non-planar results from Kalman, Rodden and Giesing,<sup>17</sup>*

All of the examples presented above considered essentially planar lifting surface cases. The vortex lattice method can also be used for highly non-planar analysis, and the example cases used at Douglas Aircraft Company in a classic paper<sup>17</sup> have been selected to illustrate the capability. To avoid copyright problems, several of the cases were re-computed using the Virginia Tech code **JKayVLM**, and provide an interesting comparison with the original results from Douglas. Figure 6-29 presents an example of the prediction capability for the pressure loading on a wing. In this case the geometry is complicated by the presence of a wing fence. The pressures are compared with data on the inboard and outboard sides of the fence. The agreement is very good on the inboard side. The comparison is not so good on the outboard side of the fence. This quality of agreement is representative of the agreement that should be expected using vortex lattice methods at low Mach numbers in cases where the flow would be expected to be attached.

Figure 6-30 provides an example of the results obtained for an extreme non-planar case: the ring, or annular, wing. In this case the estimates are compared with other theories, and seen to be very good. The figure also includes the estimate of  $C_{mq}$ . Although not included in the present discussion,  $C_{mq}$  and  $C_{lp}$  can be computed using **vlm** methods, and this capability is included in the vortex lattice method provided here, **VLMpc**.

copyrighted figure from the AIAA *Journal of Aircraft*

Figure 6-29. Comparison of  $C_p$  loading on a wings with a fence (Ref. 17).

copyrighted figure from the AIAA *Journal of Aircraft*

Figure 6-30. Example of aerodynamic characteristics of a ring wing (Ref. 17).

Figure 6-31 provides an example of the effects of the presence of the ground on the aerodynamics of simple unswept rectangular wings. The lift and pitching moment slopes are presented for calculations made using **JKayVLM** and compared with the results published by Kalman, Rodden and Giesing,<sup>17</sup> and experimental data. The agreement between the data and calculations is excellent for the lift curve slope. The  $AR = 1$  wing shows the smallest effects of ground proximity because of the three dimensional relief provided around the wing tips. As the aspect ratio increases, the magnitude of the ground effects increases. The lift curve slope starts to increase rapidly as the ground is approached.

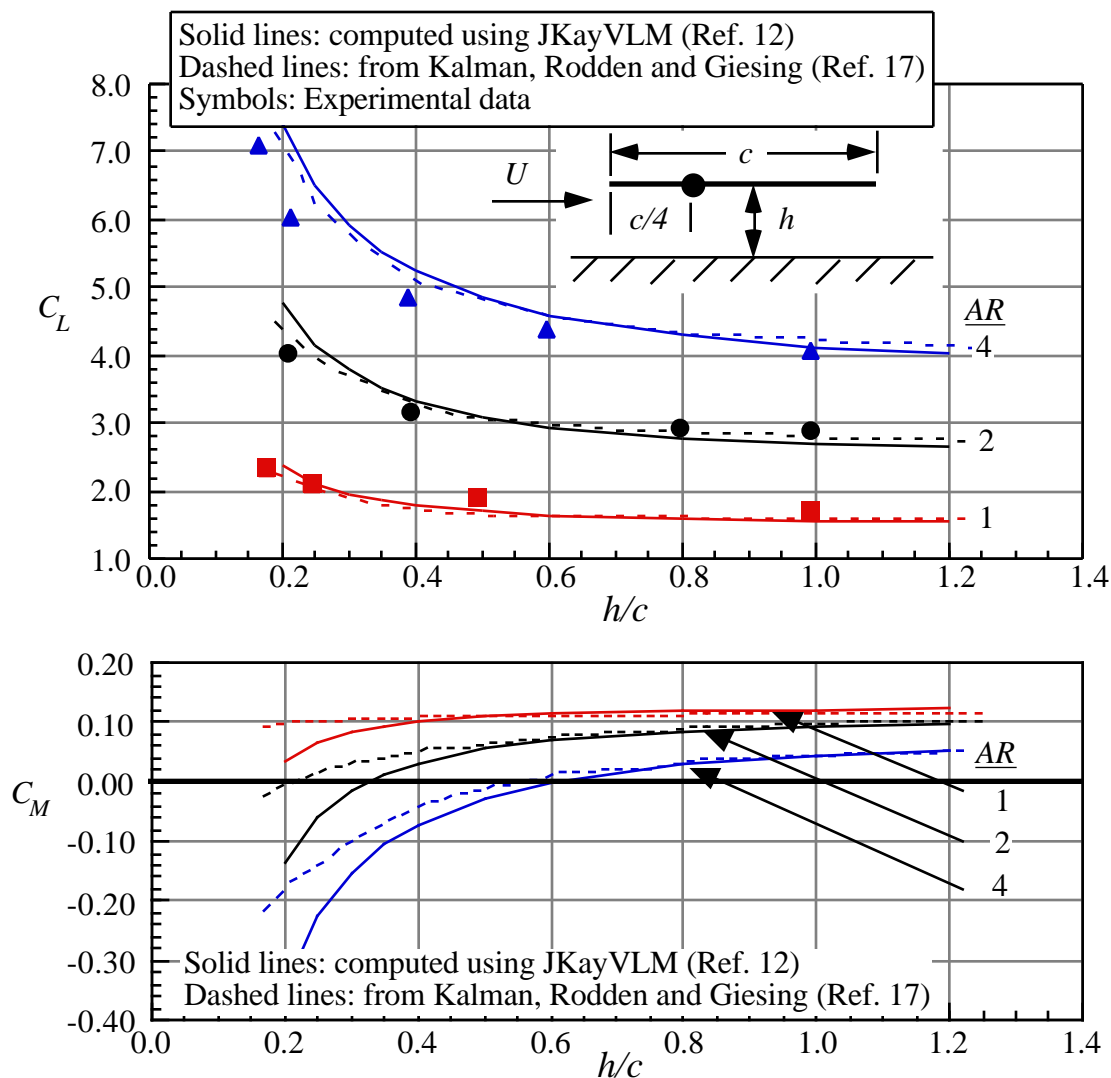


Figure 6-31. Example of ground effects for a simple rectangular wing (a case from Ref. 17).

The wings also experience a significant change in the pitching moment slope (aerodynamic center shift), and this is also shown. Note that the predictions start to differ as the ground is approached. **JKayVLM** actually rotates the entire surface to obtain another solution to use in estimating the lift curve slope. The standard procedure used by most methods is to simply change the slope condition at the mean line, as discussed previously in this chapter. Because of

the proximity to the ground, this might be a case where the transfer of the boundary condition may not be accurate. I have not asked Joe Giesing if he remembers how these calculations were made (nearly 30 years ago!).

Figure 6-32 presents similar information for the effect of dihedral angle on a wing. In this case the effects of anhedral, where the wing tip approach the ground, are extremely large. The results of dihedral changes for a wing out of ground effect are shown for comparison. Both methods agree well with each other, with differences appearing only as the wingtips approach the ground. Here again, **JKayVLM** actually rotates the entire geometry, apparently resulting in an increase in the effects as the tips nearly contact the ground. It also prevents calculations from being obtained as close to the ground as the published results. In making these calculations it was discovered that the wing panel was rotated and not sheared, so that the projected span decreases as the dihedral increases, and this produces much more pronounced changes in the lift curve slope due to the reduction in projected span.

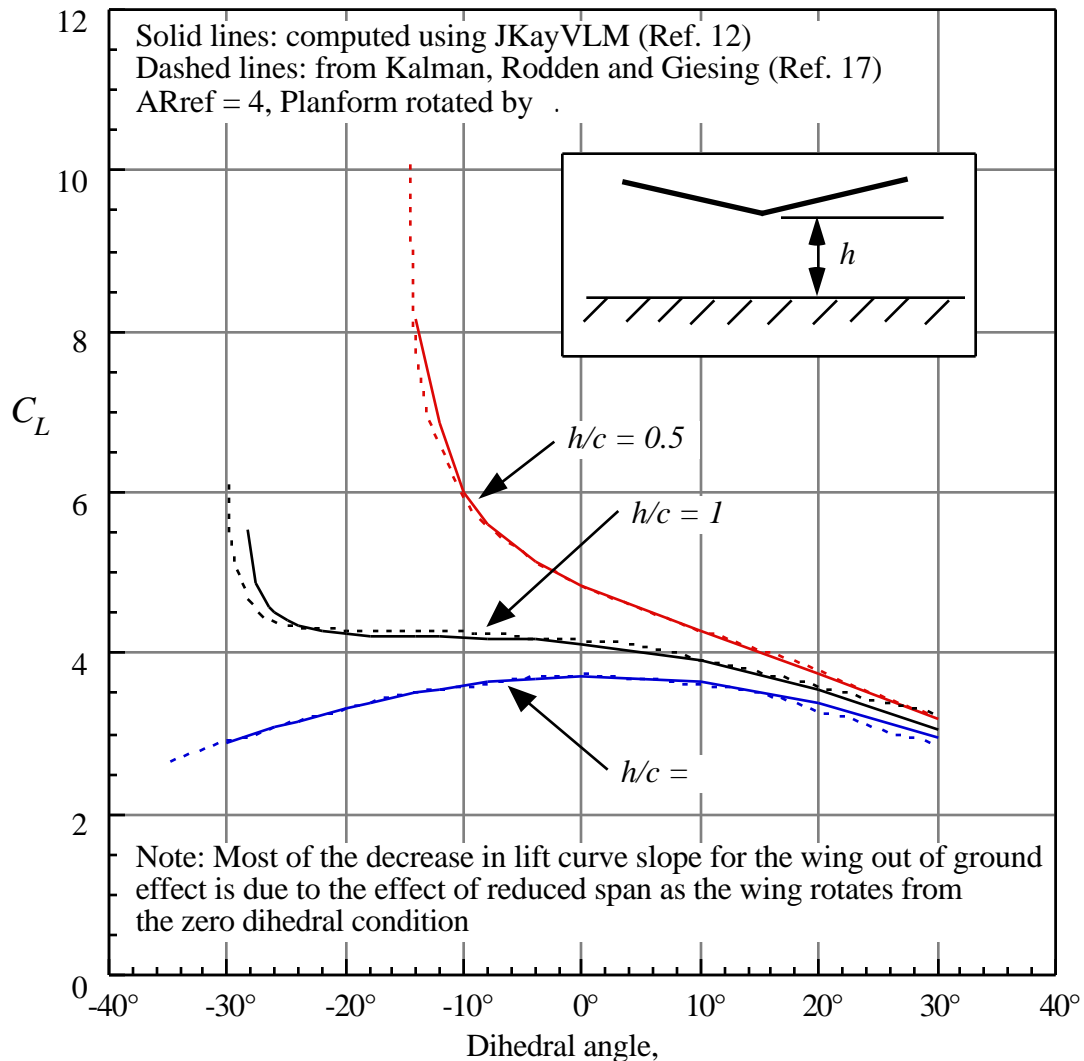


Figure 6-32. Example of ground effects for a wing with dihedral (a case from Ref. 17).

### 6.9 Program VLMpc and the Warren 12 Test Case

This vortex lattice method can be used on personal computers. The version of the Lamar program described in NASA TN D-7921<sup>3</sup> fits easily into personal computers, and is available for student use (students typed this code in from the listing in the TN) as **VLMpc**. The code and input instructions are described in Appendix D.6.

This code is still used in advanced design work, and can be used to investigate many ideas in wing aerodynamics. As shown above, results can be obtained and used before the large time consuming methods of CFD are used to examine a particular idea in detail.

This section defines one reference wing case that is used to check the accuracy of vortex lattice codes. It provides a ready check case for the evaluation of any new or modified code, as well as a check on the panel scheme layout. This wing is known as the Warren 12 planform, and is defined, together with the “official” characteristics from previous calculations, in Fig. 6-33 below.

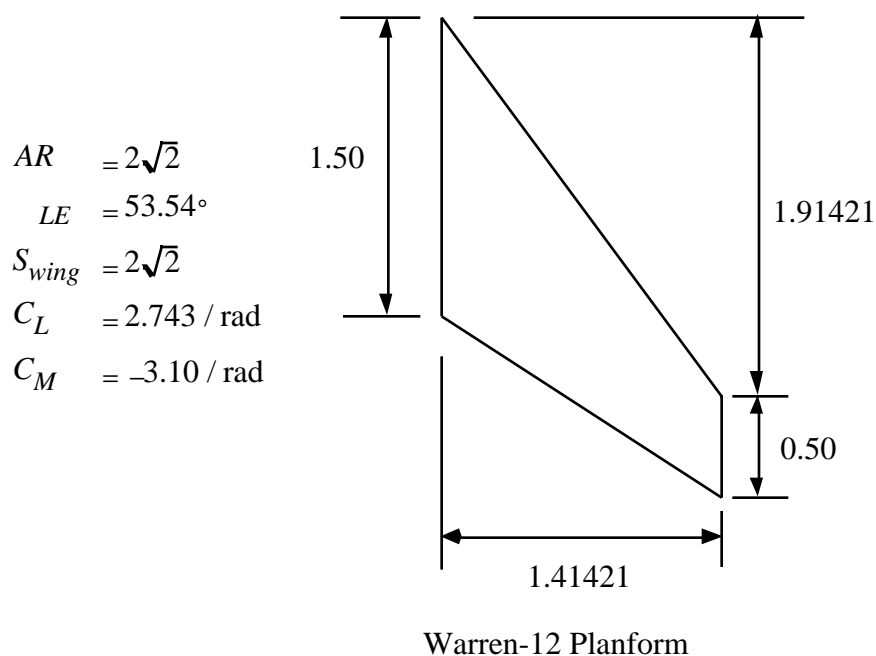


Figure 6-33. Definition and reference results for the Warren-12 wing.

For the results cited above, the reference chord used in the moment calculation is the average chord (slightly nonstandard, normally the reference chord used is the mean aerodynamic chord) and the moment reference point is located at the wing apex (which is also nonstandard).

## 6.10 Aerodynamics of Wings

With a three-dimensional method available, we can examine the aerodynamics of wings. Most of the results presented in this section were computed using **VLMpc**. One key advantage of the vortex lattice method compared to lifting line theory is the ability to treat swept wings. Classical Prandtl lifting line theory is essentially correct for unswept wings, but is completely erroneous for swept wings. Aerodynamics of unswept wings are closely related to the airfoil characteristics of the airfoil used in the wing. This relationship is less direct for swept wings. Many of the most important wing planform-oriented characteristics of wings arise when the planforms are swept. Even though sweep is used primarily to reduce compressibility effects, the important aerodynamic features of swept wings can be illustrated at subsonic speeds using the **vlm** method.

### 6.10.1 - Basic Ideas

Wings are designed to satisfy stability and handling characteristics requirements, while achieving low drag at the design conditions (usually cruise and sustained maneuver). They must also attain high maximum lift coefficients to meet field performance and maneuver requirements. Although these requirements might at first appear overwhelming, a small number of key characteristics can provide a basic physical understanding of the aerodynamics of wings.

*Aerodynamic Center:* The first key characteristic is the aerodynamic center of the wing, defined as location at which  $dC_m/dC_L = 0$ . The neutral point of the configuration is the aerodynamic center for the entire configuration. The **vlm** method was shown to provide accurate predictions of the neutral point for many configurations in the previous sections. The location of the neutral point is important in initial configuration layout to position the wing and any longitudinal stability and control surfaces at the proper location on the aircraft. Subsequently this information is fundamental in developing the control system. Wing planform shaping, as well as positioning, is used to control the location of the configuration neutral point.

*Spanload:* The next key consideration is the spanload distribution,  $cc_l/c_a$ , where  $c$  is the local chord,  $c_a$  is the average chord, and  $c_l$  is the local section lift coefficient. The spanload controls the location of the maximum section lift coefficient, the induced drag, and the magnitude of the wing root bending moment. The location and value of the maximum section lift coefficient determines where the wing will stall first.\* If the wing airfoil stalls in front of a control surface, control will be poor at flight conditions where the control becomes very important. The shape of the spanload, together with the actual value of the wingspan, determines the value of the induced

---

\* For a trapezoidal wing with an elliptic spanload the maximum value of the local lift coefficient occurs at  $x/c = 1 - \dots$

drag. For a specified span, the performance of the wing is evaluated by finding the value of the span efficiency factor,  $e$ , as described in Chapter 5. Finally, the wing root bending moment provides an indication of the structural loading requirements that the wing structure must be designed to accommodate. When considering the total system, the basic aerodynamic efficiency may be compromised to reduce structural wing weight. The shape of the spanload can be controlled through a combination of planform selection and wing twist. Typical twist distributions required to produce good wing characteristics are presented below.

The simplest example of planform shaping is the selection of wing aspect ratio, AR, wing taper,  $t$ , and wing sweep,  $\Lambda$ . While the aerodynamicist would like to see high values the aspect ratio, several considerations limit aspect ratio. Perhaps the most important limitation is the increase of wing structural weight with increasing aspect ratio. In addition, the lift coefficient required to maximize the benefits of high aspect ratio wings increases with the square root of the aspect ratio. Hence, airfoil performance limits can restrict the usefulness of high aspect ratios, especially for highly swept wings based on airfoil concepts. In recent years advances in both aerodynamics and structures have allowed aircraft to be designed with higher aspect ratios and reduced sweep. Table 6-3 provides some key characteristics of transport wings designed to emphasize efficient cruise while meeting takeoff and landing requirements.

*Taper:* Several considerations are used in selecting the wing taper. For a straight untwisted, unswept wing, the minimum induced drag corresponds to a taper ratio of about 0.4. However, a tapered wing is more difficult and hence expensive to build than an untapered wing. Many general aviation aircraft wings are built with no taper (all ribs are the same, reducing fabrication cost, and the maximum section  $C_l$  occurs at the root, well away from the control surface). To reduce structural weight the wing should be highly tapered, with  $t < .4$ . However, although highly tapered wings are desirable structurally, the section lift coefficient near the tip may become high. This consideration limits the amount of taper employed (current jet transports use taper ratios in the range of 0.2 to 0.3, as well as progressively increasing twist upward from the tip). As an example, the Aero Commander 500 had an aspect ratio of 9.5 and a taper ratio of 0.5 (it also had  $-6.5^\circ$  of twist and the quarter chord of the wing was swept forward  $4^\circ$ ).

*Sweep:* Sweep is used primarily to delay the effects of compressibility and increase the drag divergence Mach number. The Mach number controlling these effects is approximately equal to the Mach number normal to the leading edge of the wing,  $M_{\text{eff}} = M \cos \Lambda$ . The treatise on swept planforms by Küchemann is very helpful in understanding swept wing aerodynamics.<sup>18</sup> Aerodynamic performance is based on the wingspan,  $b$ . For a fixed span, the structural span increases with sweep,  $b_s = b/\cos \Lambda$ , resulting in a higher wing weight. Wing sweep also leads to aeroelastic problems. For aft swept wings flutter becomes an important consideration. If the wing

is swept forward, divergence is a problem. Small changes in sweep can be used to control the aerodynamic center when it is not practical to adjust the wing position on the fuselage (the DC-3 is the most famous example of this approach).

| Table 6-3<br>Typical Planform Characteristics of Major Transport Aircraft |           |       |      |               |       |
|---------------------------------------------------------------------------|-----------|-------|------|---------------|-------|
| 1st Flight                                                                | Aircraft  | W/S   | AR   | $^\circ(c/4)$ |       |
| 1957                                                                      | B707-120  | 105.6 | 7.04 | 35            | 0.293 |
| 1958                                                                      | DC-8-10   | 111.9 | 7.32 | 30            | 0.230 |
| 1963                                                                      | B707-320C | 110.0 | 7.06 | 35            | 0.250 |
| 1970                                                                      | B747-200B | 149.1 | 6.96 | 37.5          | 0.240 |
| 1970                                                                      | L-1011    | 124.4 | 8.16 | 35            | 0.200 |
| 1972                                                                      | DC-10-30  | 153.7 | 7.57 | 35            | 0.230 |
| 1972                                                                      | A300 B2   | 107.9 | 7.78 | 28            | 0.230 |
| 1982                                                                      | A310-100  | 132.8 | 8.80 | 28            | 0.260 |
| 1986                                                                      | B767-300  | 115.1 | 7.99 | 31.5          | 0.182 |
| 1988                                                                      | B747-400  | 149.9 | 7.61 | 37.5          | 0.240 |
| 1990                                                                      | MD-11     | 166.9 | 7.57 | 35            | 0.230 |
| 1992                                                                      | A330      | 119.0 | 9.3  | 29.74         | 0.192 |

data courtesy of Nathan Kirschbaum

To understand the effects of sweep, the Warren 12 wing is compared with wings of the same span and aspect ratio, but unswept and swept forward. The planforms are shown in Figure 6-34. The wing leading edge sweep of the aft swept wing becomes the trailing edge sweep of the forward swept wing. Figure 6-35 provides the spanload and section lift coefficient distributions from **VLMpc**. The spanload,  $cc_l / c_a$ , is given in Fig. 6-35a, where,  $c$  is the local chord,  $c_l$  is the local lift coefficient, based on the local chord, and  $c_a$  is the average chord,  $S/b$ . Using this nomenclature, the area under the curve is the total wing lift coefficient. Note that sweeping the wing aft increases the spanload outboard, while sweeping the wing forward reduces the spanload outboard. This follows directly from a consideration of the vortex lattice model of the wing. In both cases, the portion of the wing aft on the planform is operating in the induced upwash flowfield of the wing ahead of it, resulting in an increased spanload. Figure 6-35b shows the corresponding value of the local lift coefficient. Here the effect of sweep is more apparent. The forward swept wing naturally results in a spanload with a nearly constant lift coefficient. This means that a comparatively higher wing lift coefficient can be achieved before the wing stall begins. The program **LIDRAG** can be used to compare the span  $e$ 's associated with these spanloads (an exercise for the reader).

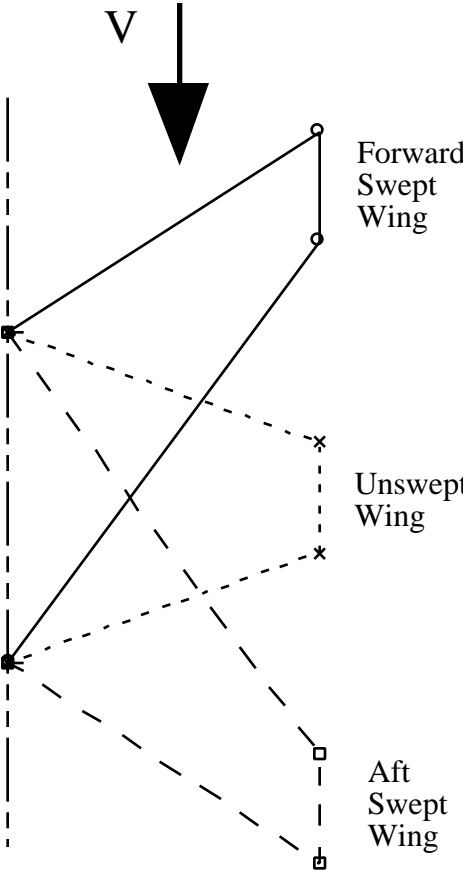
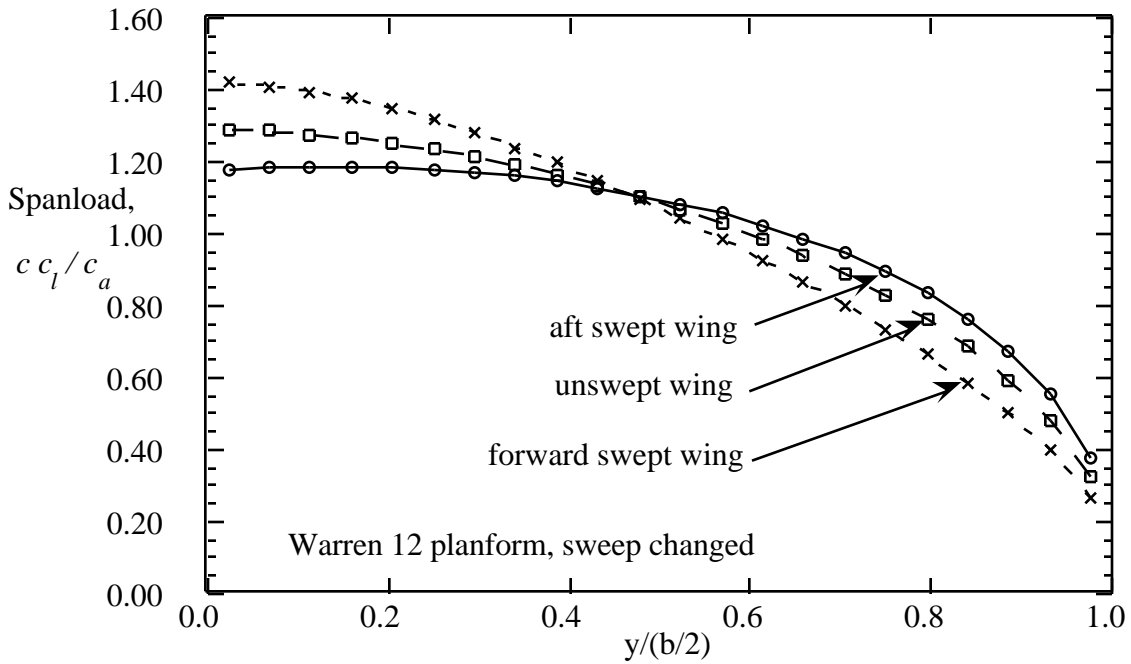
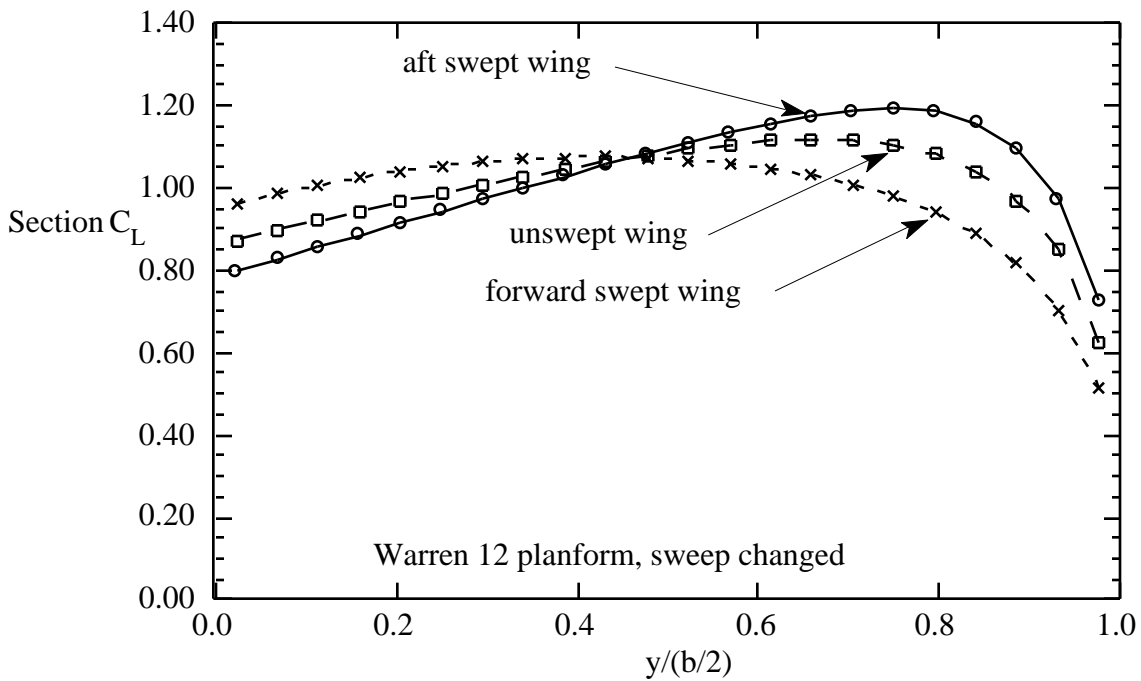


Figure 6-34. Comparison of forward, unswept, and aft swept wing planforms,  $AR = 2.8$ .



a) comparison of spanloads



b) comparison of section lift coefficients

Figure 6-35. Effects of sweep on planform spanload and lift coefficient distributions,  $AR = 2.8$ .

Similar results are now presented for a series of wings with larger aspect ratios ( $AR = 8$ ) than the wings used in the study given above. Figure 6-36 shows the planforms used for comparison, and Figure 6-37 presents the results for the spanwise distribution of lift and section lift coefficient. These results are similar to the previous results. However, the trends observed above are in fact exaggerated at the higher aspect ratio.

Aerodynamic problems as well as structural penalties arise when using a swept wing. Because of the high section lift coefficient near the tip, aft swept wings tend to stall near the tip first. Since the lift at the tip is generated well aft, the pitching moment characteristics change when this stall occurs. With the inboard wing continuing to lift, a large positive increase in pitching moment occurs when the wingtip stalls. This is known as *pitchup*, and can be difficult to control, resulting in unsafe flight conditions. Frequently the swept wing pitching moment characteristics are compounded by the effects of flow separation on the outboard control surface. Figure 6-38 provides an example of the pitching moment characteristics of an isolated aspect ratio 10 wing using experimental data.<sup>19</sup> The figure also includes the predictions from **VLMpc**. The agreement is reasonably good at low angle of attack, but deteriorates at high angle of attack as viscous effects become important. This is another reason that sweep is minimized.

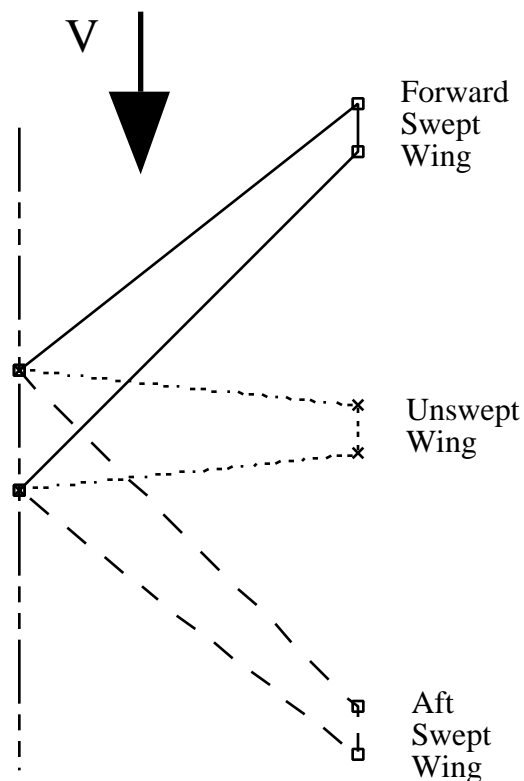
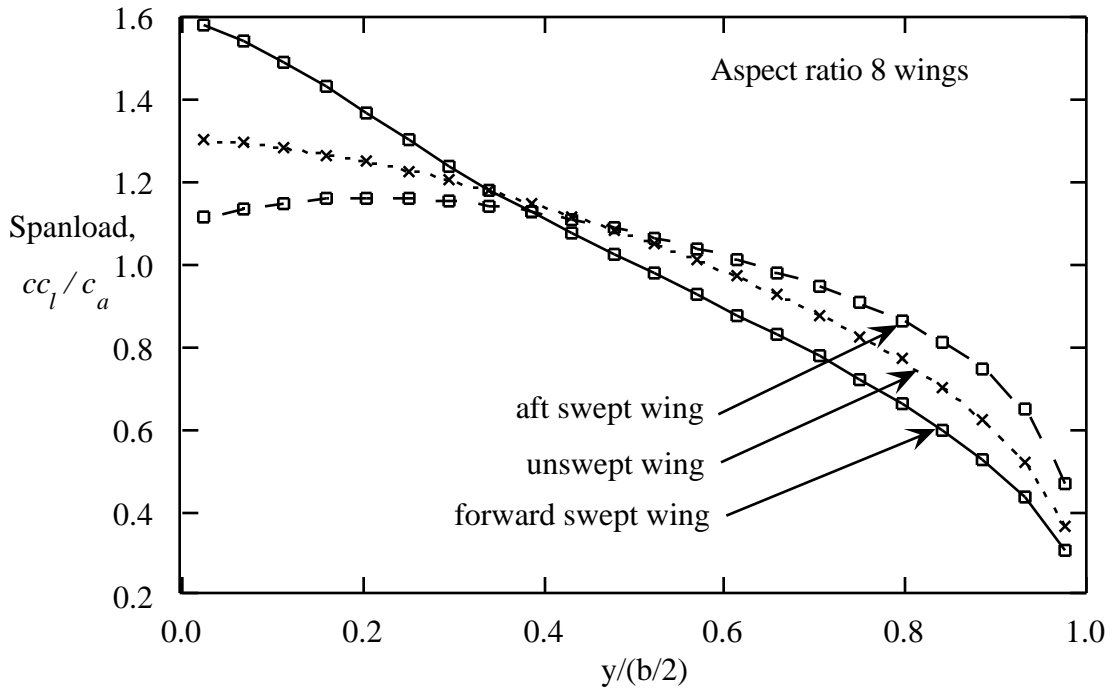
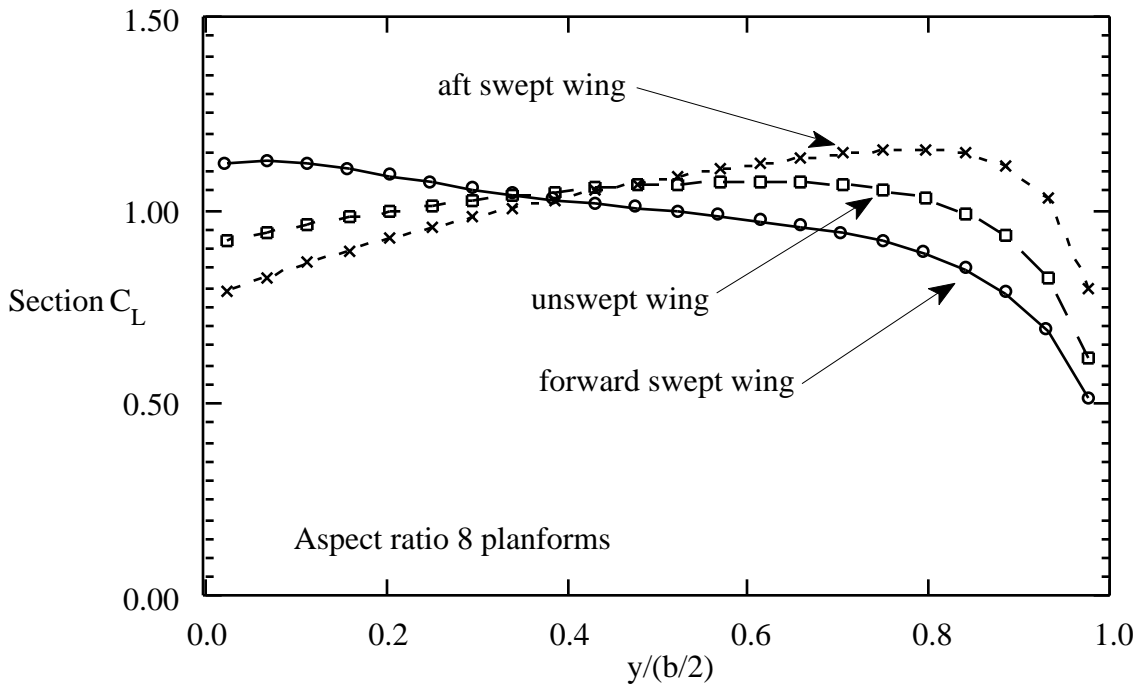


Figure 6-36. Comparison of forward, unswept, and aft swept wing planforms,  $AR = 8$ .



a) comparison of spanloads



b) comparison of section lift coefficients

Figure 6-37. Effects of sweep on planform spanload and lift coefficient distributions,  $AR = 8$ .

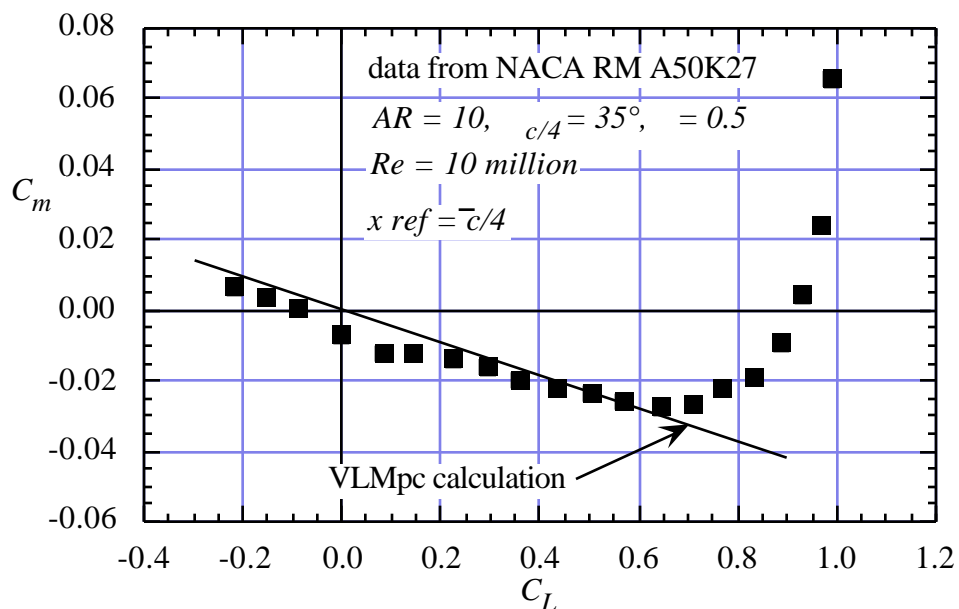


Figure 6-38. Example of isolated wing pitchup: NACA data<sup>19</sup> compared with VLMpc.

To control the spanload, the wing can be twisted. Figure 6-39 shows typical twist distributions for aft and forward swept wings, obtained from John Lamar's program **LamDes**.<sup>20</sup> (see Chapter 5 for a description). In each case the twist is used to reduce the highly loaded areas, and increase the loading on the lightly loaded portions of the wing. For an aft swept wing this means the incidence is increased at the wing root, known as washin, and reduced, known as washout, at the wing tip. Just the reverse is true for the forward swept wing. The sudden drop in required twist at the tip for the forward swept wing case is frequently seen in typical design methods and attribute to a weakness in the method and "faired out" when the aerodynamicist gives his design to the lofting group.

Although geometric sweep is used to reduce the effective Mach number of the airfoil, the geometric sweep is not completely effective. The flowfield resists the sweep. In particular, the wing root and tip regions tend to effectively unsweep the wing. Aerodynamicists study lines of constant pressure on the wing planform known as isobars to investigate this phenomenon. Figure 6-40 presents the computed isobars for a typical swept wing,<sup>21</sup> using a transonic small disturbance method.<sup>22</sup> The effect is dramatic. The effective sweep may actually correspond to the isobar line from the wing root trailing edge to the leading edge at the wing tip. To increase the isobar sweep, in addition to geometric sweep and twist, the camber surface and thickness are typically adjusted to move the isobars forward at the wing root and aft at the wing tip. This is a key part of the aerodynamic wing design job, regardless of the computational methodology used to obtain the predicted isobar pattern.

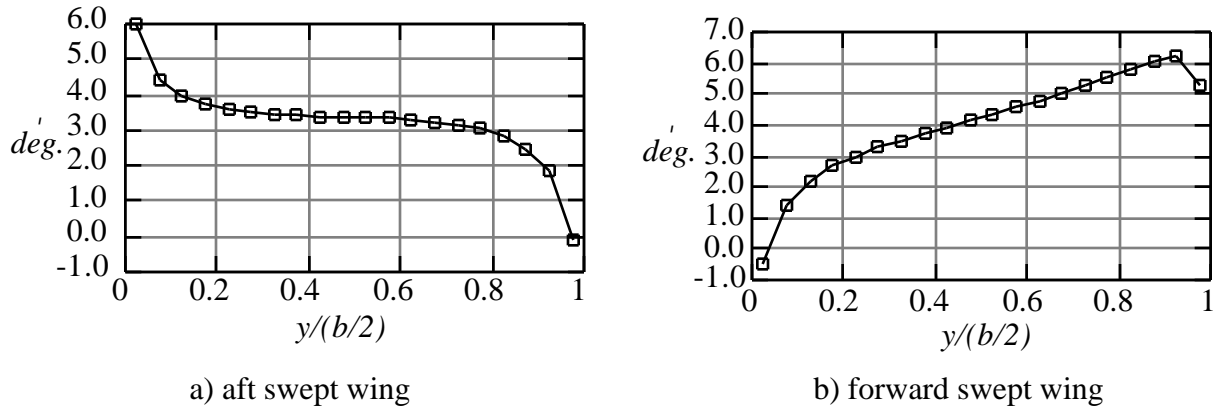


Figure 6-39. Typical twist distribution required to improve spanload on swept wings

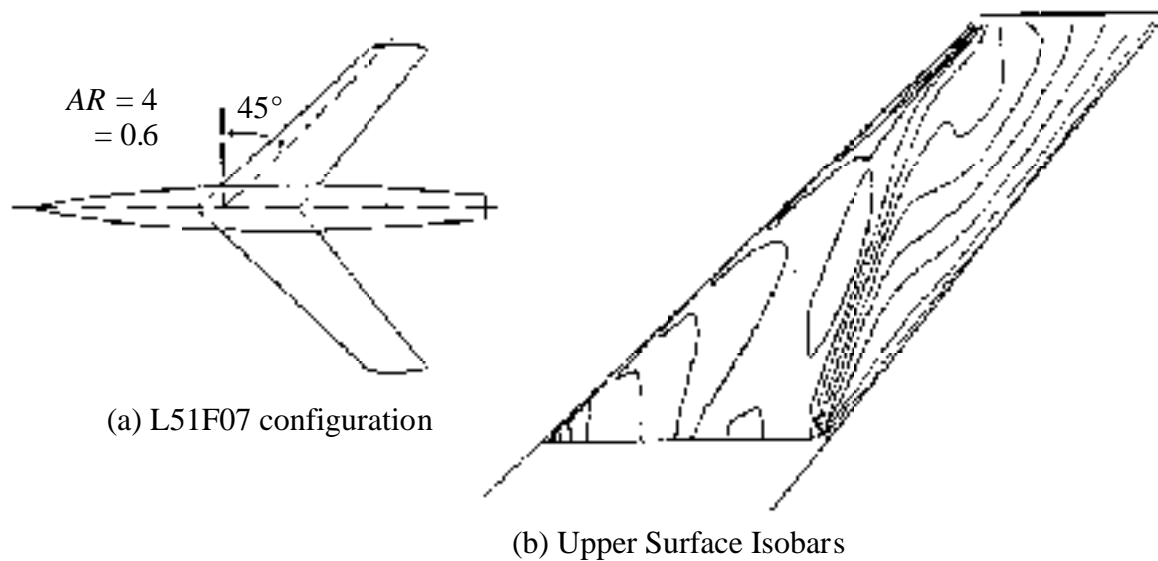


Figure 6-40. Example of the isobar distribution on an untwisted swept wing.<sup>22</sup>

Using the wing planform and twist, together with a constant chord loading, Fig. 6-41 provides the camber lines required to support the load near the root, the mid-span and the wing tip. These results were also computed using **LamDes**.<sup>20</sup> At each station a similar chord load is specified. Here we clearly see the differences in the camber required. This is an explicit illustration of the modification to an airfoil camberline required to maintain two-dimensional airfoil-type performance when the airfoil is placed in a swept wing. These modifications represent the explicit effects of the three dimensionality of the flowfield.

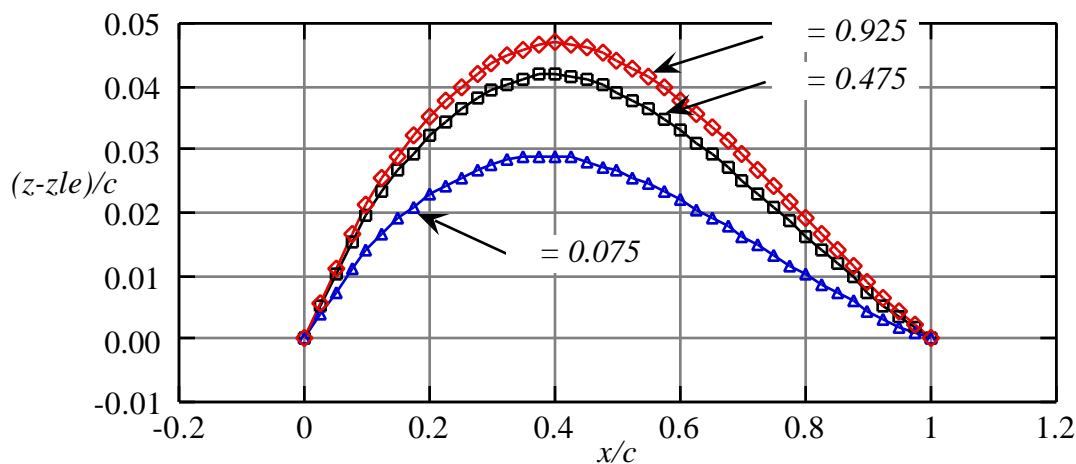


Figure 6-41. Comparison of camber lines required to develop the same chord load shape at the root, mid-span and tip region of an aft swept wing. (from **LamDes**<sup>20</sup>)

Many other refinements are available to the aerodynamic designer. Insight into both the human and technical aspects of wing design prior to the introduction of computational aerodynamics is available in two recent books describing the evolution of the Boeing series of jet transports.<sup>23,24</sup> One interesting refinement of swept wings has been the addition of trailing edge area at the wing root. Generally known as a “Yehudi flap”, this additional area arises for at least two reasons. The reason cited most frequently is the need to provide structure to attach the landing gear at the proper location. However, the additional chord lowers the section lift coefficient at the root, where wing-fuselage interference can be a problem, and the lower required section lift makes the design job easier. Douglas introduced this planform modification for swept wings on the DC-8, while Boeing did not incorporate it until the -320 model of the 707. However, the retired Boeing engineer William Cook, in his book,<sup>23</sup> on page 83, says it was first introduced on the B-29 to solve an interference problem between the inboard nacelle and the fuselage. The aerodynamic benefit to the B-29 can be found in the paper by Snyder.<sup>25</sup> Cook says, in a letter to me, that the device got its name because each wind tunnel part needed a name and there was a popular radio show at the time that featured the continuing punch line “Who’s Yehudi?” (the Bob Hope Radio show featuring Jerry Colonna, who had the line). Thus, a Boeing engineer decided to call it a Yehudi flap. This slight extra chord is readily apparent when examining the B-29, but is very difficult to photograph.

### 6.10.2 The Relation Between Airfoils and Swept Wings

Chapter 4 examined the basic aerodynamics of airfoils using panel methods. This chapter has emphasized the planform shape, and its analysis using vortex lattice methods. The connection between the airfoil and planform is important. In most cases the integration of the airfoil concept and the wing planform concept is crucial to the development of a successful configuration. Simple sweep theory can be used to provide, at least approximately, the connection between the airfoil and the planform. The typical aerodynamic design problem for an airfoil in a wing is defined by specifying the streamwise thickness to chord ratio,  $t/c$ , the local section lift coefficient,  $C_{Ldes}$ , and the Mach number. This three-dimensional problem is then converted to a corresponding two-dimensional problem. The desired two dimensional airfoils are then designed and transformed back to the streamwise section to be used as the wing airfoil section. Examples of the validity of this technique, together with details on other properties, including the “cosine cubed” law for profile drag due to lift are available in the NACA report by Hunton.<sup>26</sup> The relations between the streamwise airfoil properties and the chordwise properties (values normal to the leading edge, as shown in Fig. 6-42) are:

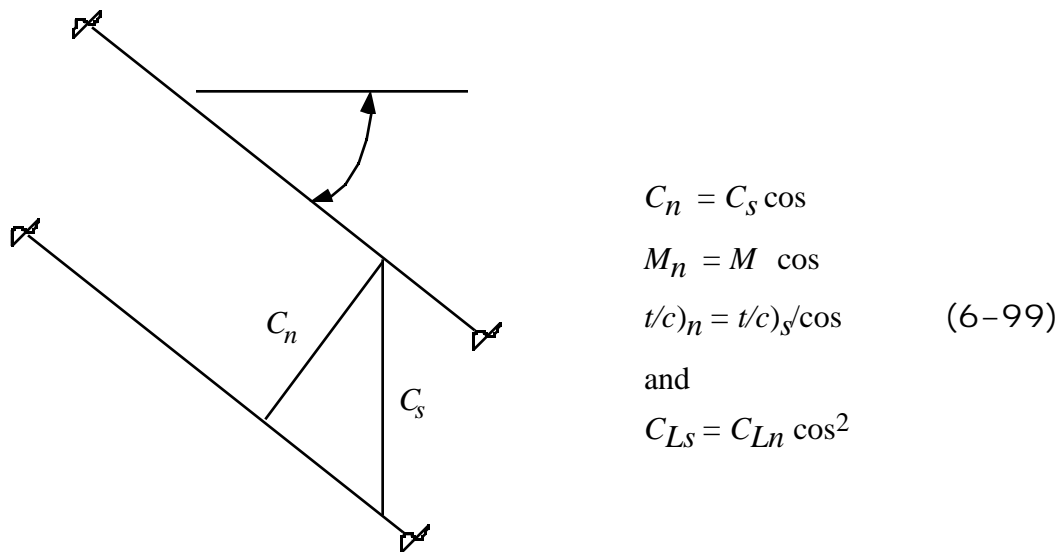


Figure 6-42. Swept wing definitions.

These relations demonstrate that the equivalent two-dimensional airfoil is thicker, operates at a lower Mach number, and at a higher lift coefficient than the three dimensional wing airfoil section. Taper effects on real wings require the selection of an effective sweep angle. Numerous approaches have been used to determine the effective angle, where guidance has been obtained by examining experimental data. The quarter chord sweep or shock sweep are typical choices.

One good example of airfoil/planform matching is the Grumman X-29. In that case wind tunnel testing of advanced transonic maneuver airfoil sections on aft swept wing configurations led the aerodynamicists (Glenn Spacht in particular) to conclude that the proper planform to take advantage of the advanced airfoil section performance should be swept forward.

### 6.10.3 - Wing/Tail and Canard/Wing Aerodynamics

Additional lifting surfaces are used to provide control over a wide range of conditions. If modern advanced control systems are not used, the extra surface is also designed, together with the rest of the configuration, to produce a stable design. Considering aft tail configurations first, the problem of pitchup described above for isolated wings must be reconsidered for aft tailed configurations. In particular, T-tail aircraft can encounter problems when the horizontal tail interacts with the wake of the wing at stall. Figure 6-43 provides the pitching moment characteristics of the DC-9.<sup>27</sup> The initial abrupt nose-down characteristic is the result of careful design, before the large pitchup develops. Note that even though pitch-up is a viscous effect, inviscid calculations clearly show why it happens, and can provide valuable information.

Figure 6-43 shows that a stable trim condition occurs at an angle of attack of  $43^\circ$ . This is an undesirable equilibrium condition, which could result in the vehicle actually trying to “fly” at this angle of attack. If adequate control power is not available, it may even be difficult to dislodge the vehicle from this condition, which is commonly known as a *deep* or *hung stall*. This will result in a rapid loss of altitude due to the very high drag. Although for this configuration full down elevator eliminates the possibility of getting “trapped” in a trimmed flight condition at this angle of attack, the amount of pitching moment available may not be sufficient to affect a rapid recovery from this condition. Examples of pitchup characteristics are not readily available. Aerodynamic designers do not like to admit that their configurations might have this characteristic. This aspect of swept wing and wing-tail aerodynamics is an important part of aerodynamic configuration development.

Even low tail placement cannot guarantee that there will not be a problem. Figure 6-44 shows the pitching moment characteristics for an F-16 type wind tunnel model.<sup>28</sup> In this case a deep stall is clearly indicated, and in fact the allowable angle of attack on the F-16 is limited to prevent the airplane from encountering this problem. In this case the pitchup arises because of powerful vortices generated by the strakes, which continue to provide lift as the wing stalls. This type of flowfield is discussed in Section 6.12.

Canard configurations provide another interesting example of multiple lifting surface interaction. The downwash from the canard wake, as it streams over the wing, reduces the effective angle of attack locally, and hence the local lift on the wing behind the canard. Wing

twist is used to counteract this effect. Figure 6-45 illustrates how this interaction occurs. The relative loading of the surfaces is an important consideration in configuration aerodynamics. The induced drag is highly dependent on the relative wing loading, which is determined by the selection of the configuration stability level and the requirement to trim about the center of gravity. In determining the induced drag, Figure 6-46, also computed using **LamDes**,<sup>20</sup> shows how the trimmed drag changes with  $cg$  position. Three different canard heights are shown for a range of  $cg$  positions, which is equivalent to varying the stability level. Figure 6-47 provides an example of the wing twist required to account for the effect of the canard downwash. Note that the forward swept wing twist increment due to the canard acts to reduce the twist required, which is exactly opposite the effect for the aft swept wing.

a copyrighted figure from the AIAA *Journal of Aircraft*

Figure 6-43. Pitching moment characteristics of the DC-9.<sup>27</sup>

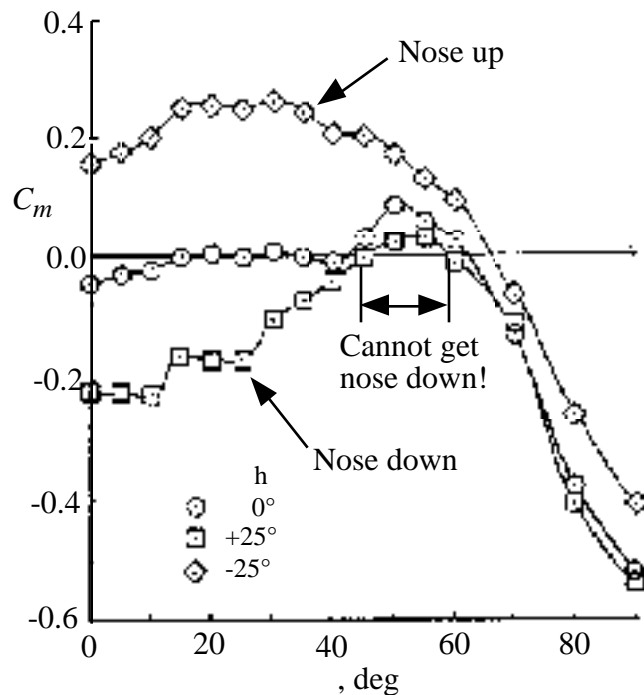


Figure 6-44. Pitching moment characteristics of an F-16 type wind tunnel model.<sup>28</sup>

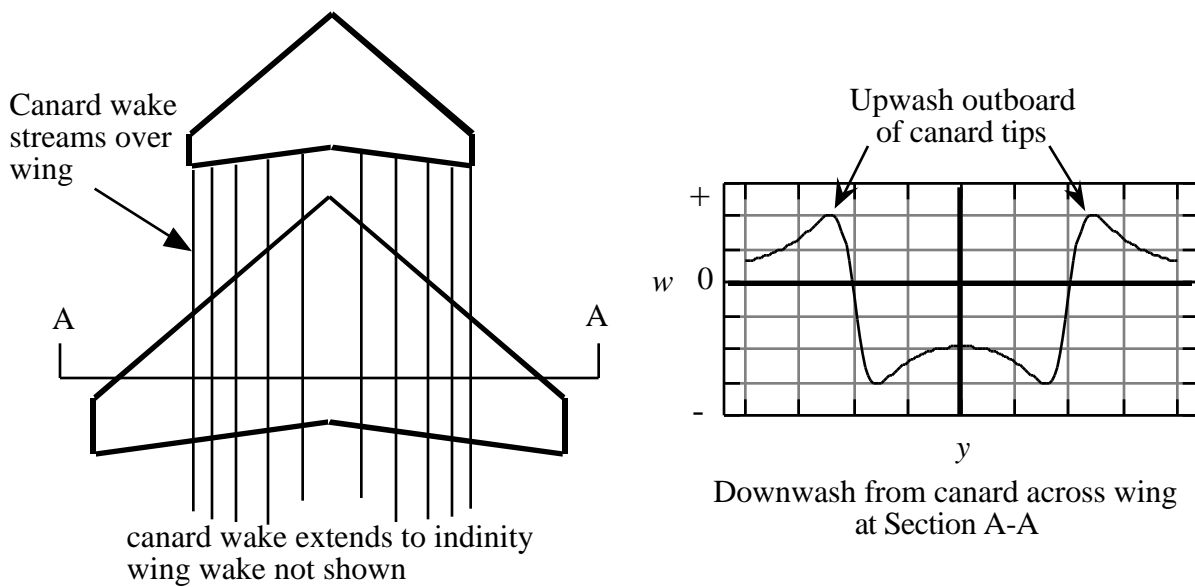
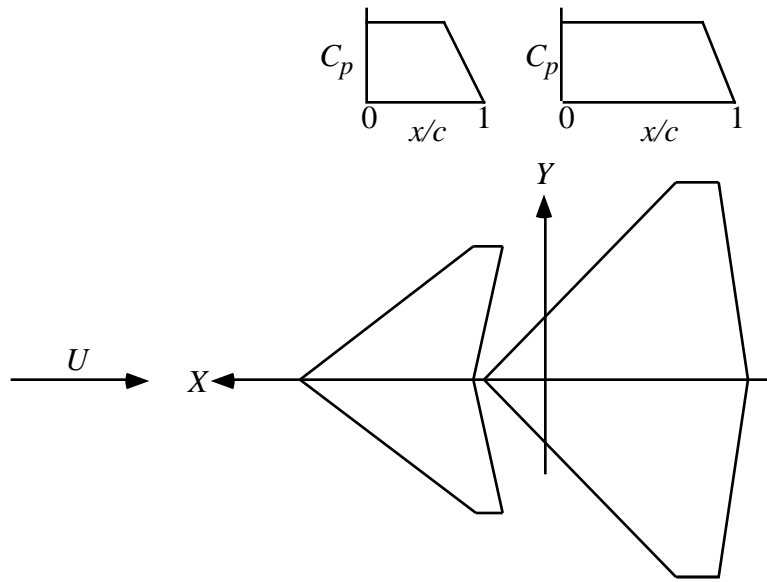
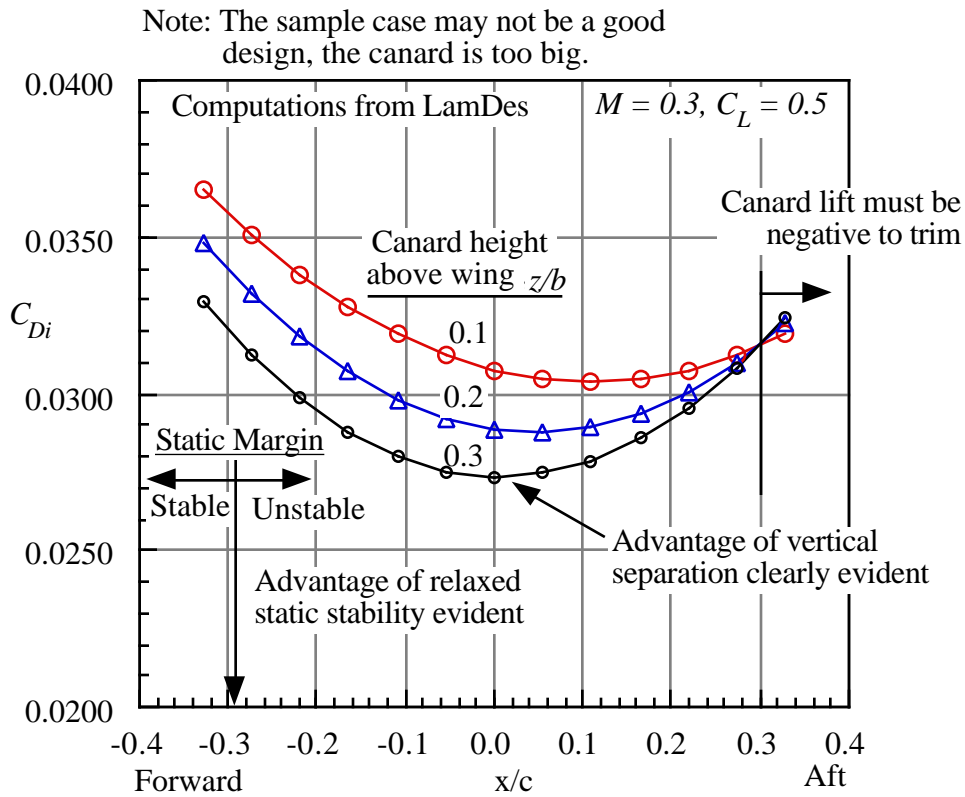


Figure 6-45. Illustration of wing-canard interaction.



a) Canard-wing planform and chord loads used in drag calculation.



b) Minimum trimmed drag variation with trim position and canard-wing separation.

Figure 6-46. Example of relation of minimum trimmed drag to balance (stability).<sup>20</sup>

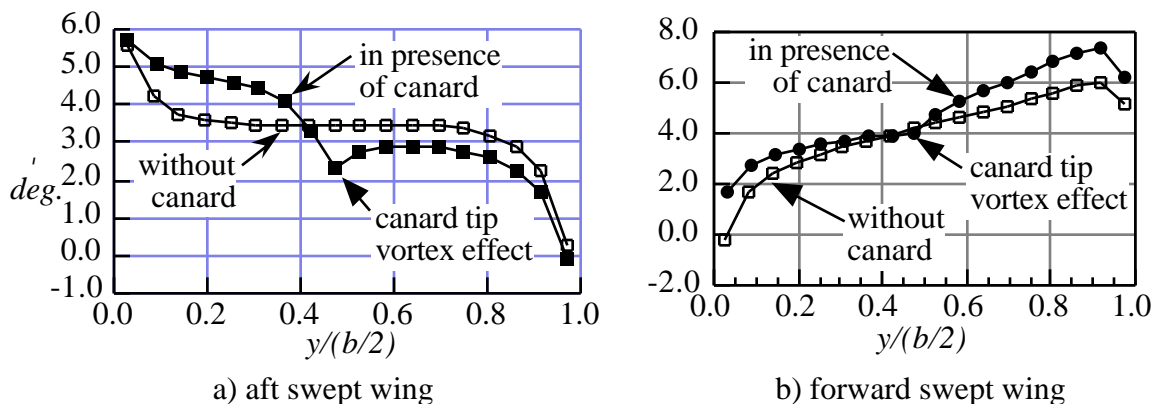


Figure 6-47. Effects of canard on twist requirements. Twist required for minimum drag using LamDes<sup>20</sup> (Note: results depend on configuration details, balance).

### 6.11 Inverse Design Methods and Program DesCam

Although most of the analysis discussed above corresponds to the analysis problem, the design problem can also be treated. In this section we provide one example: the determination of the camber line shape required to obtain a specific chord load in the two dimensional case. We take the opportunity to illustrate a method due to Lan<sup>6</sup> that uses a mathematically based selection of vortex and control point placements instead of the 1/4 - 3/4 rule used above.

Recall that a line of vortex singularities induces a vertical velocity on the singularity line given by (see chapter 4 and Karamcheti<sup>13</sup>):

$$w(x) = -\frac{1}{2} \int_0^c \frac{\gamma(x')}{x - x'} dx' . \tag{6-100}$$

For thin wing theory the vertical velocity can be related to the slope as shown above in Section 6.2. The vortex strength can be related to the streamwise velocity by  $\gamma = u^+ - u^-$ . This in turn can be used to relate the vorticity to the change in pressure,  $C_p$  through:

$$C_p = C_{p_l} - C_{p_u} = -2u^- - 2u^+ = 2(u^+ - u^-) \tag{6-101}$$

which leads to:

$$\frac{C_p(x)}{2} = \gamma(x) \tag{6-102}$$

resulting in the expression for camber line slope in terms of design chord load:

$$\frac{dz}{dx} = -\frac{1}{4} \int_0^c \frac{C_p(x')}{x - x'} dx' . \tag{6-103}$$

Here  $dz/dx$  includes the slope due to the angle of attack. Note that the integral contains a singularity, and this singularity introduces the extra complications that require special analysis for numerical integration. The original Lan theory was used to find  $C_p$  (in a slightly different form), but it can also be used to obtain  $dz/dx$  from  $C_p$ . To do this, Lan derived a summation formula to obtain the slope. Once the slope is known, it is integrated to obtain the camber line.

Lan showed that the integral in Eq. (6-100) could be very accurately found from the summation:

$$\left. \frac{dz}{dx} \right|_i = -\frac{1}{N} \sum_{k=1}^N \frac{C_p}{4} \frac{\sqrt{x_k(1-x_k)}}{x_i - x_k} \quad (6-104)$$

where:

$$x_k = \frac{1}{2} \left[ 1 - \cos \frac{(2k-1)\pi}{2N} \right] \quad k = 1, 2, \dots, N \quad (6-105)$$

and:

$$x_i = \frac{1}{2} \left[ 1 - \cos \frac{i\pi}{N} \right] \quad i = 0, 1, 2, \dots, N. \quad (6-106)$$

Here  $N + 1$  is the number of stations on the camber line at which the slopes are obtained.

Given  $dz/dx$ , the camber line is then computed by integration using the trapezoidal rule (marching forward starting at the trailing edge):

$$z_{i+1} = z_i - \frac{x_{i+1} - x_i}{2} \left( \left. \frac{dz}{dx} \right|_i + \left. \frac{dz}{dx} \right|_{i+1} \right). \quad (6-107)$$

The design angle of attack is then:

$$\alpha_{DES} = \tan^{-1} z_0 \quad (6-108)$$

The camber line can then be redefined in standard nomenclature, i.e.,  $z(x=0) = z(x=1) = 0.0$ :

$$\bar{z}_i = z_i - (1 - x_i) \tan \alpha_{DES} \quad (6-109)$$

How well does this work? Program **DesCam** implements the method described here, and the user's manual is provided in App. D.7. Here we compare the results from **DesCam** with the analytic formula given in Appendix A.1 for the NACA 6 Series mean line with  $a = .4$ . The results are shown in Figure 6-48 below. Notice that the camber scale is greatly enlarged to

demonstrate the excellent comparison. Even though the chord load is constructed by two straight line segments, the resulting required camber line is highly curved over the forward portion of the airfoil. Note also that thin airfoil theory allows only two possible values for the pressure differential at the leading edge, zero or infinity. A close examination of the camber line shape required to produce a finite load reveals a singularity. The slope is infinite. This feature is much easier to study using the analytic solution, as given in Appendix A. This approach can easily be extended to three dimensions. Notice that design problem is direct, in that it does not require the solution of a system of equations.

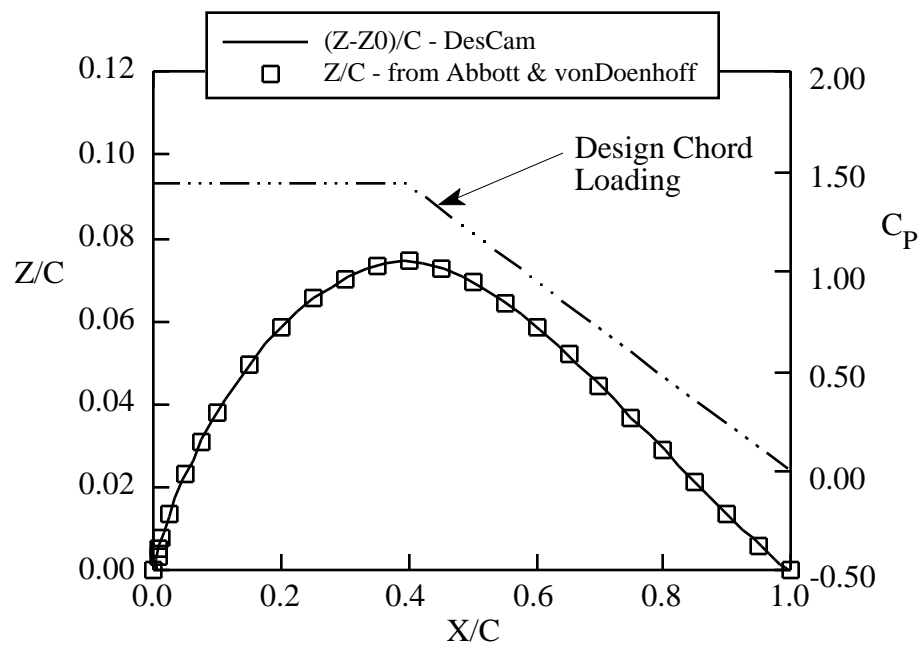


Figure 6-48. Example and verification of camber design using **DesCam**.

## 6.12 Vortex Flow Effects and the Leading Edge Suction Analogy

For highly swept wings at even moderate angles of attack, the classical attached flow/trailing edge Kutta condition flow model we've adopted is wrong. Instead of the flow remaining attached on the wing and leaving the trailing edge smoothly, the flow separates at the leading edge, forming a well defined vortex. This vortex plays an important role in the design of highly swept, or "slender wing" aircraft. The most notable example of this type of configuration is the Concorde. Sharp leading edges promote this flow phenomena. The basic idea is illustrated in the sketch from Payne and Nelson<sup>29</sup> given here in Fig. 6-49.

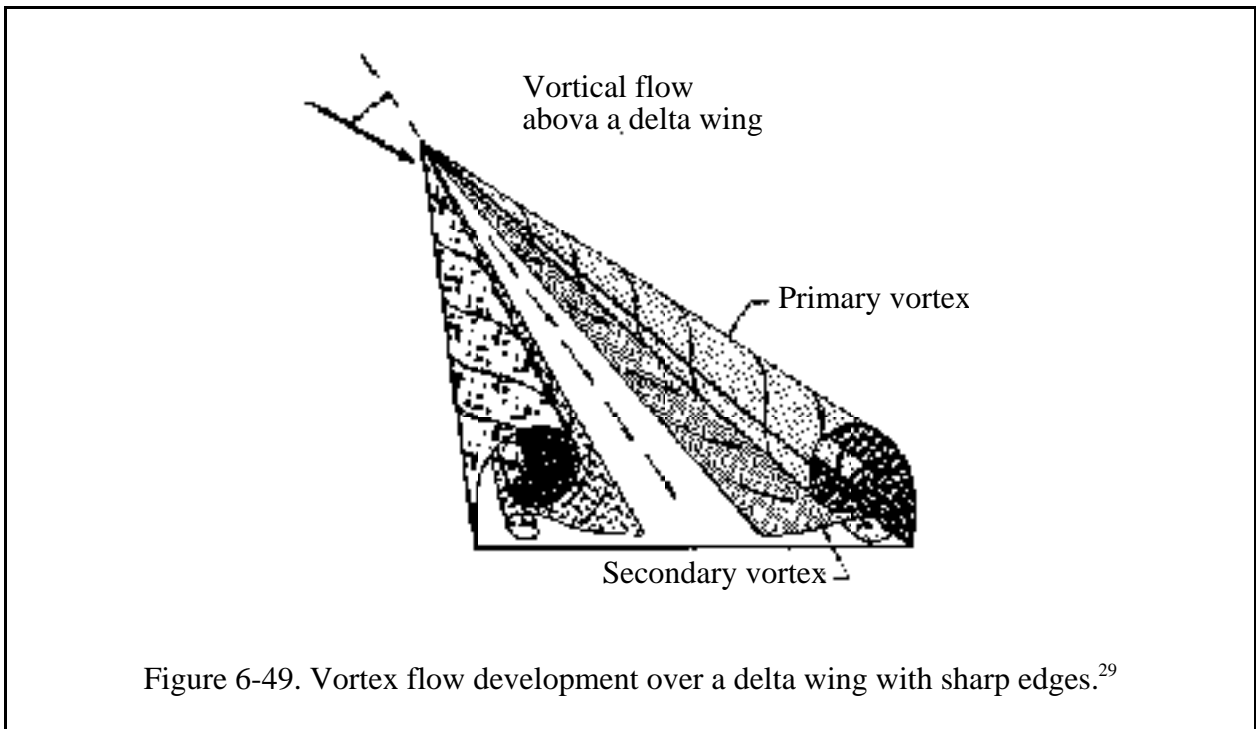
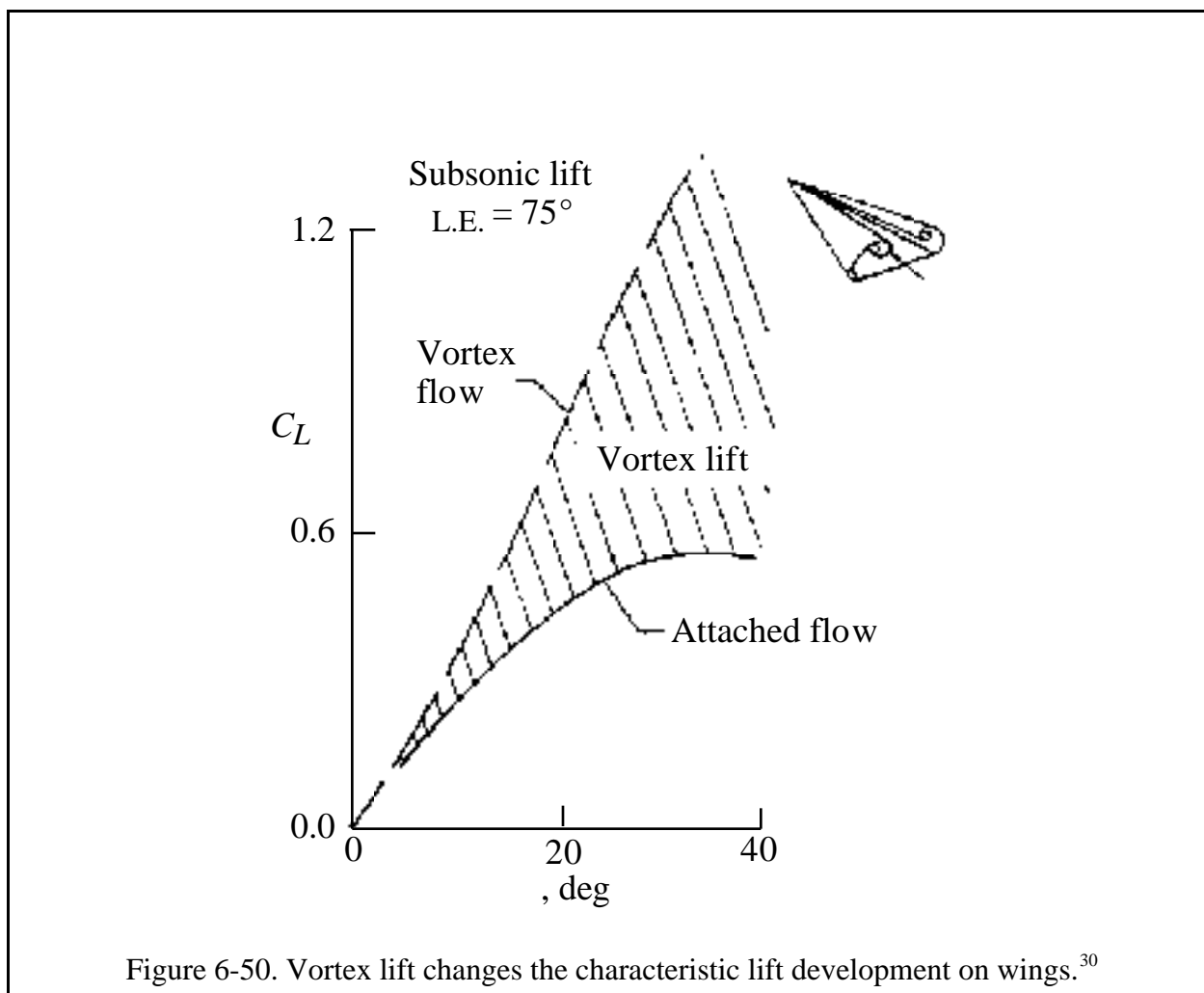


Figure 6-49. Vortex flow development over a delta wing with sharp edges.<sup>29</sup>

An important consequence of this phenomena is the change in the characteristics of the lift generation as the wing angle of attack increases. The vortex that forms above the wing provides an additional low pressure force due to the strongly spiraling vortex flow. The low pressure associated with the centrifugal force due to the vortex leads to the lower pressure on the wing surface. As the wing increases its angle of attack the vortex gets stronger, further reducing the pressure on the wing. The resulting increase in lift due to the vortex can be large, as shown in Fig. 6-50, from Polhamus.<sup>30</sup>

This is an important flow feature. Slender wings have very low attached flow lift curve slopes, and without the additional vortex lift it would be impractical to build configurations with low aspect ratio wings. The low attached flow alone lift curve slope would prevent them from being able to land at acceptable speeds or angle of attack. Vortex lift made the Concorde possible. Another feature of the flow is the high angle of attack at which maximum lift occurs,

and typically a very mild lift loss past maximum lift. These features are a direct result of the leading edge vortex flow structure that occurs on slender wings.



Although the vortex lattice method formulation presented above does not include this effect, vortex lattice methods are often used as the basis for extensions that *do* include the leading edge vortex effects. A remarkable, reasonably accurate, flow model for leading edge vortex flows was introduced by Polhamus<sup>31,32</sup> at NASA Langley in 1966 after examining lots of data. This flow model is known as the “Leading Edge Suction Analogy.” The concept is quite simple and was invented for sharp edged wings. The leading edge suction that should exist according to attached flow theory (see section 5.8) is assumed to rotate 90° and generate a vortex induced force instead of a suction when leading edge vortex flow exists. Thus the vortex flow force is assumed to be equal to the leading edge suction force. However, the force now acts in the direction normal to the wing surface in the direction of lift rather than in the plane of the wing leading edge. The concept is shown in the Fig. 6-51 from the original Polhamus NASA report.<sup>31</sup> Further details on the effects of vortex flow effects are also available in the reports by Kulfan.<sup>33,34</sup>

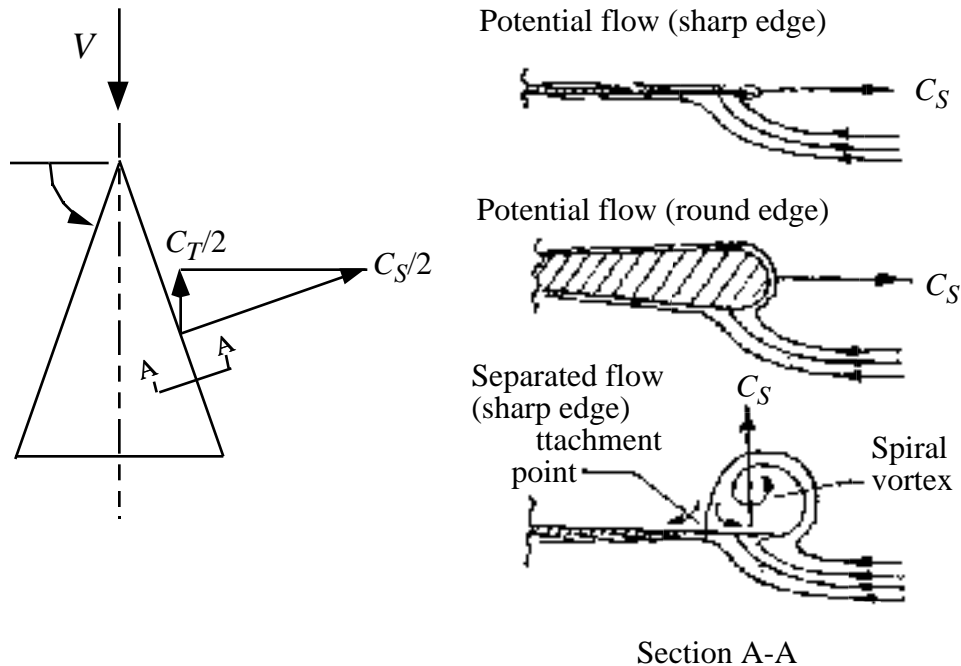


Figure 6-51. The Polhamus leading edge suction analogy.

Polhamus developed charts to compute the suction force for simple wing shapes. For a delta wing with a sharp leading edge, the method is shown compared with the data of Bartlett and Vidal<sup>35</sup> in Figure 6-52. The agreement is quite good (my reconstruction doesn't show agreement as good as that presented by Polhamus,<sup>31</sup> but it is still impressive).

The figure also shows the large size of the vortex lift, and the nonlinear shape of the lift curve when large angles are considered. This characteristic was exploited in the design of the Concorde.

To find the vortex lift using the leading edge suction analogy, an estimate of the leading edge suction distribution is required. However the suction analogy does not result in an actual flowfield analysis including leading edge vortices. The Lamar vortex lattice code (**VLMpc**) optionally includes a fully developed suction analogy based on Polhamus ideas, with extensions to treat side edge suction by John Lamar<sup>3</sup> also included.

Other approaches have been developed to compute leading edge vortex flows in more detail. Many of these methods allow vortex filaments, simulating the leading edge vortices, to leave the leading edge. The location of these vortices, and their effect on the wing aerodynamics as they roll up are explicitly computed. Mook<sup>10</sup> and co-workers are leaders in this methodology.

The area of vortex flows in configuration aerodynamics is fascinating, and an entire conference was held at NASA Langley<sup>36</sup> devoted to the topic. The references cited above were selected to provide an entry to the literature of these flows. Interest in the area remains strong. The effects of round leading edges have been investigated by Ericsson and Reding<sup>37</sup> and Kulfan.<sup>33</sup> The relation between sweep, vortex lift, and vortex strength has been given recently by Hemsch and Luckring.<sup>38</sup>

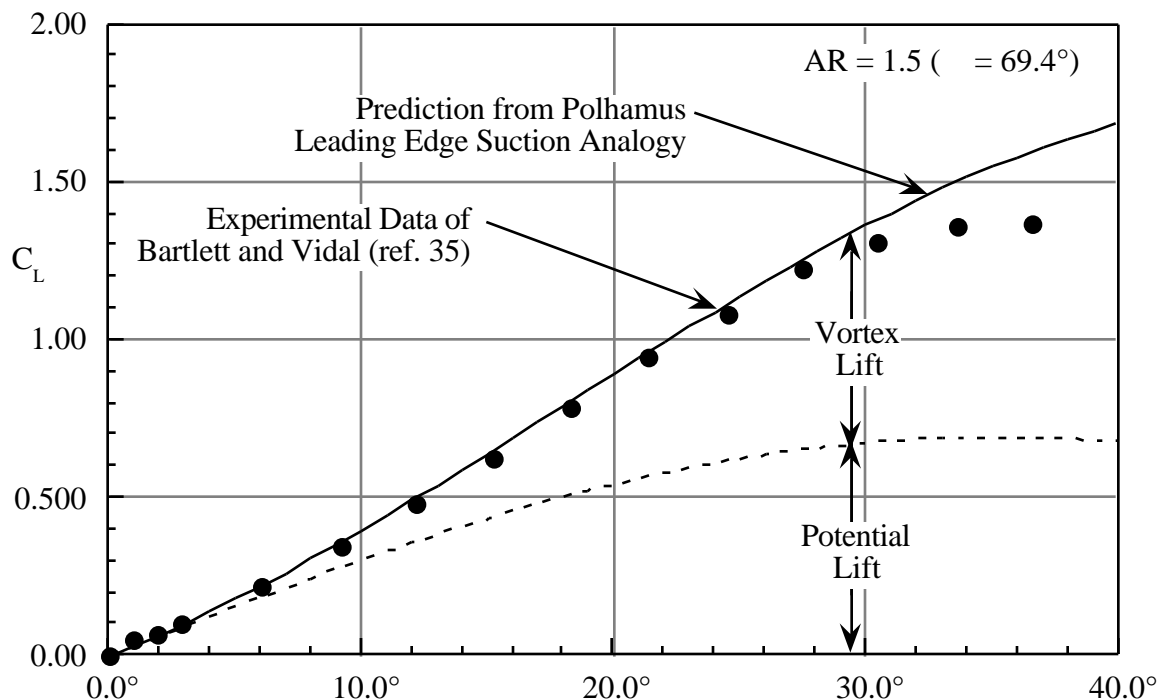


Figure 6-52. Comparison of the leading edge suction analogy with data.

### 6.13 Alternate and Advanced VLM Methods

Many variations of the vortex lattice method have been proposed. They address both the improvement in accuracy for the traditional case with a planar wake, and extensions to include wake position and rollup as part of the solution. Areas requiring improvement include the ability to predict leading edge suction, the explicit treatment of the Kutta condition, and the improvement in convergence properties with increasing numbers of panels.<sup>8</sup> The traditional vortex lattice approaches assume that the wing wake remains flat and aligned with the freestream. This assumption is acceptable for most cases. The effect of the wake on the wing that generates it is small unless the wing is highly loaded. However, the interaction between the wake from an upstream surface and a trailing lifting surface can be influenced by the rollup and position.

In the basic case where the wake is assumed to be flat and at a specified location, the primary extensions of the method have been directed toward improving the accuracy using a smaller number of panels. Hough<sup>7</sup> demonstrated that improvement in accuracy could be achieved by using a lattice that was slightly smaller than the true planform area. Basically, he proposed a 1/4 panel width inset from the tips.

Perhaps the most important revision of the vortex lattice method was proposed by Lan<sup>6</sup>, and called the “quasi vortex lattice method.” In this method Lan used mathematical methods, rather than the more heuristic arguments described above, to find an approximation for the thin airfoil integral in the streamwise direction. The result was, in effect, a method where the vortex and control point locations were established from the theory of Chebychev polynomials to obtain an accurate estimate of the integrals with a small number of panels. The mathematically based approach also led to an ability to compute leading edge suction very accurately.

The wake rollup and position problem has been addressed by Mook<sup>10</sup> among others, and his work should be consulted for details. A method similar to Mook’s has been presented recently in the book by Katz and Plotkin.<sup>11</sup> They propose a vortex ring method, which has advantages when vortices are placed on the true surface of a highly cambered shapes.

#### *Unsteady flow extension*

Analogous extensions have been made for unsteady flow. For the case of an assumed flat wake the extension to harmonically oscillating surfaces was given by Albano and Rodden.<sup>39</sup> When the vortex is augmented with an oscillating doublet, the so-called *doublet-lattice method* is obtained. The doublet-lattice method is widely used for subsonic flutter calculations. Kalman, Giesing and Rodden<sup>17</sup> provide additional details and examples (they also included the steady flow examples given above).

General unsteady flows calculations, including wake location as well as the incorporation of leading edge vortices, have been carried out by Mook among others. The resulting codes have the potential to be used to model time accurate aerodynamics of vehicles in arbitrary maneuvering flight, including the high angle of attack cases of interest in fighter aerodynamics. These codes are currently being used in studies where the aircraft aerodynamics is coupled with advanced control systems. In this case the active control is incorporated and the dynamics of the maneuver change dramatically due to the incorporation of a stability and control augmentation system.

#### *To sum up*

The summary provided above illustrates the current state of affairs. Vortex lattice methods, *per se*, are not being developed. However, they are being used in advanced methods where several disciplines are being studied simultaneously and an affordable model of the aerodynamics is required.

### 6.14 Exercises

1. Get a copy of **VLMpc** from the web site. The detailed instructions for this program are included in Appendix D.6. Install the program on your personal computer and repeat the sample case, checking that your output is the same as the sample output files on the web. Study the output to familiarize yourself with the variety of information generated. Turn in a report describing your efforts (*not* the output), including any mods required to make the code run on your computer.
2. How good is thin airfoil theory? Compare the thin airfoil theory  $C_p$  for a 2D flat plate airfoil with program **VLMpc**.

Flat plate thin airfoil theory:

$$C_p = 4 \sqrt{\frac{(1 - x/c)}{x/c}}$$

- i. Pick an aspect ratio 10 unswept wing at  $\alpha = 3^\circ$  and  $12^\circ$  and run **VLMpc**.
  - ii. Plot  $(C_p)/\sqrt{x/c}$  as a function of  $x/c$  at the wing root.
  - iii. How many panels do you need to get a converged solution from VLM?
  - iv. What conclusions do you reach?
3. Compare the validity of an aerodynamic strip theory using **VLMpc**. Consider an uncambered, untwisted wing,  $AR = 4$ ,  $\alpha = 4^\circ$ ,  $l_e = 50^\circ$ , at a lift coefficient of 1. Plot the spanload, and the  $C_p$  distribution at approximately the center section, the midspan station, and the 85% semispan station. Compare your results with a spanload constructed assuming that the wing flow is approximated as 2D at the angle of attack required to obtain the specified lift. Also compare the chordloads,  $C_p$ , at the three span stations. How many panels do you need to obtain converged results. Document your results. Do you consider this aerodynamic strip theory valid based on this investigation? Comment.
  4. Compare the wing aerodynamic center location relative to the quarter chord of the  $mac$  for the wing in exercise 3, as well as similar wings. Consider one wing with zero sweep on the quarter chord, and a forward swept wing with a leading edge sweep of  $-50^\circ$ . Compare the spanloads. Document and analyze these results. What did you learn from this comparison?
  5. For the wings in exercise 4, compare the section lift coefficients. Where would each one stall first? Which wing appears to be able to reach the highest lift coefficient before the section stalls.
  6. For the problem in exercise 5, add twist to each wing to obtain near elliptic spanloads. Compare the twist distributions required in each case.
  7. Pick a NASA or NACA report describing wind tunnel results for a simple one or two lifting surface configuration at subsonic speeds. Compare the lift curve slope and stability level predicted by **VLMpc** with wind tunnel data. Submit a report describing your work and assessing the results.
  8. Add a canard to the aft and forward swept wings analyzed in exercise 4. Plot the sum of the spanloads. How does the canard effect the wing spanload.
  9. Consider the wings in exercise 8. How does lift change with canard deflection? Add an equivalent tail. Compare the effect of tail or canard deflection on total lift and moment. Did you learn anything? What?
  10. Construct a design code using the 1/4 - 3/4 rule and compare with **DESCAM**.
  11. Construct a little 2D code to study ground effects.
  12. Compare wing and wing/tail(canard) results for  $C_L$  with standard analytic formulas.

## 6.15 References

- <sup>1</sup> *Vortex Lattice Utilization* Workshop, NASA SP-405, May, 1976
- <sup>2</sup> Margason, R.J., and Lamar, J.E., "Vortex-Lattice FORTRAN Program for Estimating Subsonic Aerodynamic Characteristics of Complex Planforms," NASA TN D-6142, 1971
- <sup>3</sup> Lamar, J.E., and Gloss, B.B., "Subsonic Aerodynamic Characteristics of Interacting Lifting Surfaces With Separated Flow Around Sharp Edges Predicted by a Vortex-Lattice Method," NASA TN D-7921, 1975
- <sup>4</sup> Lamar, J.E., and Herbert, H.E., "Production Version of the Extended NASA-Langley Vortex Lattice FORTRAN Computer Program," Vol. I, User's Guide, (requires update packet, July, 1984) NASA TM 83303, 1982
- <sup>5</sup> Herbert, H.E., and Lamar, J.E., "Production Version of the Extended NASA-Langley Vortex Lattice FORTRAN Computer Program," Vol. II, Source Code, NASA TM 83304, 1982
- <sup>6</sup> Lan, C.E., "A Quasi-Vortex-Lattice Method in Thin Wing Theory", *Journal of Aircraft*, Vol. 11, No. 9, September 1974, pp. 518-527.
- <sup>7</sup> Hough, Gary R., "Remarks on Vortex-Lattice Methods," *Journal of Aircraft*, Vol. 10, No. 5, May 1973, pp. 314-317.
- <sup>8</sup> DeJarnette, F.R., "Arrangement of Vortex Lattices on Subsonic Wings," in *Vortex Lattice Utilization Workshop*, NASA SP-405, May, 1976. pp. 301-319.
- <sup>9</sup> Frink, Neal T., "Lifting-Surface Theory for Skewed and Swept Subsonic Wings," *Journal of Aircraft*, Vol. 19, No. 7, July 1982, pp. 519-524.
- <sup>10</sup> Mook, D.T., and Nayfeh, A.H., "Application of the Vortex-Lattice Method to High-Angle-of-Attack Subsonic Aerodynamics," SAE Paper No. 851817, October, 1985.
- <sup>11</sup> Katz, J., and Plotkin, A., *Low-Speed Aerodynamics: From Wing Theory to Panel Methods*, McGraw-Hill, Inc., New York, 1991.
- <sup>12</sup> Jacob Kay, W.H. Mason, W. Durham, F. Lutze and A. Benoliel, "Control Power Issues in Conceptual Design: Critical Conditions, Estimation Methodology, Spreadsheet Assessment, Trim and Bibliography," VPI-Aero-200, November 1993.
- <sup>13</sup> Karamcheti, K., *Principles of Ideal Fluid Aerodynamics*, John Wiley & Sons, New York, 1966, pp: 518
- <sup>14</sup> Bertin, J.J., and Smith, M.L., *Aerodynamics for Engineers*, Prentice-Hall, Inc., Englewood Cliffs, 2nd Ed., 1989, pp: 261-282, 3rd Ed. 1998, pp: 291-311.
- <sup>15</sup> Thomas, R.W., "Analysis of Aircraft Stability and Control Design Methods," AFWAL-TR-84-3038, Vol. II, App. B., "Evaluation of Aerodynamic Panel Methods," by John Koegler, May, 1984.
- <sup>16</sup> Pittman, J.L., and Dillon, J.L., "Vortex Lattice Prediction of Subsonic Aerodynamics of Hypersonic Vehicle Concepts," *Journal of Aircraft*, Vol. 14, No. 10, pg 1017, October, 1977.
- <sup>17</sup> Kalman, T.P., Rodden, W.P., and Giesing, J., "Application of the Doublet-Lattice Method to Nonplanar Configurations in Subsonic Flow," *Journal of Aircraft*, Vol. 8, No. 6, June 1971, pp. 406-415.
- <sup>18</sup> Küchemann, D., *The Aerodynamic Design of Aircraft*, Pergamon Press, Oxford, 1978.
- <sup>19</sup> Tinling, B.E., and Kolk, W. R., "The Effects of Mach Number and Reynolds Number on the Aerodynamic Characteristics of Several 12-Percent-Thick Wings Having 35° of Sweepback and Various Amounts of Camber," NACA RM A50K27, Feb. 1951.

- <sup>20</sup> Lamar, J.E., "A Vortex Lattice Method for the Mean Camber Shapes of Trimmed Non-Coplanar Planforms with Minimum Vortex Drag," NASA TN D-8090, June 1976.
- <sup>21</sup> Loving, D.L., and Estabrooks, B.B., "Transonic Wing Investigation in the Langley Eight Foot High Speed Tunnel at High Subsonic Mach Numbers and at Mach Number of 1.2," NACA RM L51F07, 1951.
- <sup>22</sup> Mason, W.H., MacKenzie, D.A., Stern, M.A., Ballhaus, W.F, Jr., and Frick, J., "Automated Procedure for Computing the Three-Dimensional Transonic Flow Over Wing-Body Combinations, including Viscous Effects," Vol. I, Description of Methods and Applications, AFFDL-TR-77-122, February 1978.
- <sup>23</sup> Cook, William C., *The Road to the 707*, TYC Publishing, Bellevue, 1991.
- <sup>24</sup> Irving, Clive, *Wide-Body: The Triumph of the 747*, William Morrow, New York, 1993.
- <sup>25</sup> Snyder, George, "Structural Design Problems in the B-29 Airplane," *Aeronautical Engineering Review*, Feb. 1946, pp. 9-12.
- <sup>26</sup> Hunton, Lynn W., "A Study of the Application of Airfoil Section Data to the Estimation of the High-Subsonic-Speed Characteristics of Swept Wings," NACA RM A55C23, June 1955.
- <sup>27</sup> Shevell, R.S., and Schaufele, R.D., "Aerodynamic Design Features of the DC-9," *Journal of Aircraft*, Vol. 3, No. 6, Nov.-Dec. 1966, pp. 515-523.
- <sup>28</sup> Nguyen, L.T., Ogburn, M.E., Gilbert, W.P., Kibler, K.S., Brown, P.W., and Deal, P.L., "Simulator Study of Stall/Post-Stall Characteristics of a Fighter Airplane With Relaxed Longitudinal Static Stability," NASA TP 1538, Dec. 1979.
- <sup>29</sup> Payne, F.W., and Nelson, R.C., "An Experimental Investigation of Vortex Breakdown on a Delta Wing," in *Vortex Flow Aerodynamics*, NASA CP 2416, 1985.
- <sup>30</sup> Polhamus, E.C., "Application of Slender Wing Benefits to Military Aircraft," AIAA Wright Brothers Lecture, AIAA-83-2566, 1983..
- <sup>31</sup> Polhamus, E.C., "A Concept of the Vortex Lift on Sharp Edge Delta Wings Based on a Leading-edge Suction Analogy," NASA-TN 3767, 1966.
- <sup>32</sup> Polhamus, E.C., "Prediction of Vortex Lift Characteristics by a Leading-edge Suction Analogy," *Journal of Aircraft*, Vol. 8, No. 4, 1971, pp. 193-199.
- <sup>33</sup> Kulfan, R.M., "Wing Airfoil Shape Effects on the Development of Leading-Edge Vortices," AIAA 79-1675, 1979.
- <sup>34</sup> Kulfan, R.M., "Wing Geometry Effects on Leading Edge Vortices," AIAA Paper No. 79-1872, 1979.
- <sup>35</sup> Bartlett, G.E., and Vidal, R.J., "Experimental Investigation of Influence of Edge Shape on the Aerodynamic Characteristics of Low Aspect Ratio Wings at Low Speeds," *Journal of the Aeronautical Sciences*, Vol. 22, No. 8, August, 1955, pp.517-533,588.
- <sup>36</sup> *Vortex Flow Aerodynamics*, NASA SP-2416 (volume I), and NASA SP-2417 (volume II), October, 1985.
- <sup>37</sup> Ericsson, L.E., and Reding, J.P., "Nonlinear Slender Wing Aerodynamics," AIAA Paper No. 76-19, January, 1976.
- <sup>38</sup> Hemsch, M.J., and Luckring, J.M., "Connection Between Leading-Edge Sweep, Vortex Lift, and Vortex Strength for Delta Wings," *Journal of Aircraft*, Vol. 27, No. 5, May 1990, pp. 473-475.
- <sup>39</sup> Albano, E., and Rodden, W.P., "A Doublet-Lattice Method for Calculating Lift Distributions on Oscillating Surfaces in Subsonic Flows," *AIAA J.*, Vol. 7, No. 2, February 1969, pp. 279-285; errata *AIAA J.*, Vol. 7, No. 11, November 1969, p. 2192.